Chemical Engineering Journal 441 (2022) 136023

Contents lists available at ScienceDirect

Chemical Engineering Journal

journal homepage: www.elsevier.com/locate/cej

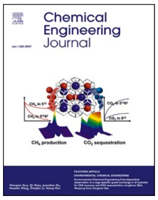

Hydrogen-rich gas production by catalytic steam gasification of rice husk using CeO_2-modified Ni-CaO sorption bifunctional catalysts

Xi Zeng [a,c], Mengxiang Fang [a,b,*], Tong Lv [a], Jianglei Tian [a,b], Zhixiang Xia [a], Jianmeng Cen [a], Qinhui Wang [a]

[a] State Key Laboratory of Clean Energy Utilization, Zhejiang University, Hangzhou 310027, China
[b] Qingshanhu Energy Research Center, Zhejiang University, Hangzhou 311300, China
[c] College of Electrical Engineering, Guizhou University, Guiyang 550025, China

ARTICLE INFO

Keywords:
Hydrogen
Rice husk
Steam gasification
Catalytic reforming
CeO_2-modified Ni-CaO sorption bifunctional catalysts
CO_2 sorption

ABSTRACT

Hydrogen-rich gas production from rice husk via steam gasification and catalytic reforming using CeO_2-modified Ni-CaO sorption bifunctional catalysts synthesized by sol–gel method in a two-stage system was investigated. The results show that the $Ce_{0.7}Ni_1Ca_5$ catalyst achieves maximum H_2 concentration (85.81(±0.39) vol.%) and H_2 yield (35.82(±0.28) mmol $g^{-1}{}_{biomass}$) under a condition of 500 °C, S/C (steam/carbon in biomass) molar ratio of 5, catalyst/biomass mass ratio of 2.5, producing the lowest content of CO_2 (3.62(±0.16) vol.%), CO (4.27(±0.11) vol.%), CH_4 (4.49(±0.18) vol.%), and C_2-C_3 (1.81(±0.09) vol.%), correspondingly. $Ce_{0.7}Ni_1Ca_5$ also exhibits excellent cyclic stability in H_2 production, CO_2 sorption, and inhibition of carbon deposition. The H_2 concentration and H_2 yield remain above 81.88 vol% and 32.11 mmol $g^{-1}{}_{biomass}$, respectively, and CO_2 emission keeps below 4.85 vol% during 10 cyclic tests. The carbon deposition of $Ce_{0.7}Ni_1Ca_5$ is only about 30% of that of Ni_1Ca_5 after 10 cycles and hardly increased after 5 cycles. It is found that well-dispersed CeO_2 can effectively prevent the sintering of NiO and delay agglomeration of CaO species, stabilizing CaO carbonation and CO_2 sorption, and the strong Ni-O-Ce interaction induces the creation of oxygen vacancies that facilitate the fracture of O–H bonds of water for the formation of H_2. Furthermore, the high oxygen transport capacity of CeO_2 not only forms abundant mesopores structure to promote WGS and SMR reactions for enhancing H_2 production, but also contributes to reforming the carbon deposited on the catalyst surface by lowering the oxidation temperature of amorphous carbon containing low-molecular aromatic or aliphatic compounds with lower degree of graphitization.

1. Introduction

Hydrogen, which is a clean fuel with three times higher energy content per unit weight of fuel (142 kJ g^{-1}) than gasoline [1], has been widely used in various fields [2–4]. Hydrogen produced from renewable energy such as biomass is a way to achieve future energy sustainability due to its carbon neutrality [5–7] and potential to mitigate climate change and environmental pollution caused by fossil fuels. Biomass is an abundant resource and provides energy requirements of about 33% and 3% in developing and developed countries, respectively [8]. Rice husk is one of the waste biomass widely used as energy feedstock. Large quantities of rice husk are produced as the main by-product of rice processing industry, the estimated worldwide production of rice husk is approximately 100 million tons per year, of which 90% are produced from developing countries [9]. The reuse of rice husk alleviates environmental problems that arise from open burning or storing [10].

Steam gasification is a thermochemical process that converts carbonaceous fuels into combustible gases, which is a common application nowadays for energy recovery from biomass [11,12]. However, this process usually produces CO_2 and requires high temperatures (700–900 °C) [2], which may aggravate the evaporation of alkali salts in biomass and cause equipment corrosion [13]. A scheme proposed to solve these problems is the sorption-enhanced steam gasification, which enhances the water–gas shift reaction (WGS, Eq. (6)) toward H_2 production owing to the in situ CO_2 sorption by CaO-based sorbents. Additionally, the CO_2 sorption temperature should be controlled at 500–650 °C considering that CO_2 desorption would happen above 800 °C [14] due to the exothermic carbonation of CaO. Therefore, gasification with CaO is usually performed at lower temperatures compared to conventional gasification process, which reduces energy

---

* Corresponding author at: State Key Laboratory of Clean Energy Utilization, Zhejiang University, Hangzhou 310027, China.
E-mail address: mxfang@zju.edu.cn (M. Fang).

https://doi.org/10.1016/j.cej.2022.136023
Received 4 January 2022; Received in revised form 27 February 2022; Accepted 23 March 2022

supply.

$Ca(OH)_2$ is cheap and widely-sourced and has been widely applied as a CaO-based sorbent for its dual functions of CO_2 sorption [15] and alkaline depolymerization of cellulose (one of three compositions of biomass, accounting for more than 44 wt% as shown in Table 1). Compared to CaO, $Ca(OH)_2$ has several advantages: firstly, direct carbonation of $Ca(OH)_2$ (Eq (1)) occurs at a lower temperature (350–400 °C). Whereupon $Ca(OH)_2$ dehydrates rapidly to CaO at around 400 °C (Eq (2)) and is followed by a continued reaction of CaO with CO_2 (Eq (3)) until the maximum carbonation is achieved. It is a significant improvement in CO_2 sorption capacity by direct carbonation of $Ca(OH)_2$ because it presents more kinetically favored than the mechanism in the sequence of dehydration followed by carbonation [16]. Secondly, the release of water during carbonation of $Ca(OH)_2$ improves its pore structure, promoting the inward diffusion and sorption of CO_2. Furthermore, the released water helps to remove possible carbon deposited on the sorbent (Eq (4)) [16]. Finally, $Ca(OH)_2$ shows a selective catalytic activity in the cleavage of C–C and C-O bonds, which depolymerizes cellulose into smaller C_4 to C_6 linear oxygenates like acids and phenols at low temperatures (< 200 °C) [17,18]. In this study, $Ca(OH)_2$ was evenly mixed with biomass for alkaline degradation of biomass and in-situ CO_2 sorption at a moderate temperature.

$$Ca(OH)_2 + CO_2 \leftrightarrow CaCO_3 + H_2O,\ \Delta H^0_{298} = -69\ \text{kJ mol}^{-1} \tag{1}$$

$$Ca(OH)_2 \leftrightarrow CaO + H_2O,\ \Delta H^0_{298} = +109\ \text{kJ mol}^{-1} \tag{2}$$

$$CaO + CO_2 \leftrightarrow CaCO_3,\ \Delta H^0_{298} = -178\ \text{kJ mol}^{-1} \tag{3}$$

$$C + H_2O \leftrightarrow CO + H_2,\ \Delta H^0_{298} = +132\ \text{kJ mol}^{-1} \tag{4}$$

A catalyst synthesized by mixing the Ni-based catalyst and CaO-based sorbent has been widely applied in sorption enhanced steam reforming [15,19,20]. A two-stage system combining gasification/pyrolysis and catalytic steam reforming has been proved to be effective to enhance gas yield, biomass conversion rates, and lower tar content [21–24]. Our previous work [25] has shown that the maximum H_2 concentration of 79.22 vol% and H_2 yield of 27.36 mmol $g^{-1}_{cellulose}$ are achieved at 500 °C in a two-stage system. The steam gasification of cellulose with $Ca(OH)_2$ occurs in the first stage as Eq. (5), then the derived gases like H_2, CO_2, CO, CH_4, light hydrocarbons, and tar are reformed by Ni-CaO catalyst in the second stage (Eqs. (6)–(8)).

$$C_xH_yO_z + Ca(OH)_2 + H_2O \rightarrow (H_2 + CH_4 + CO_2 + CO + C_xH_y \ldots) + \text{Tar} + \text{Char} + CaCO_3 \tag{5}$$

$$CO + H_2O \leftrightarrow CO_2 + H_2 \tag{6}$$

$$CH_4 + H_2O \leftrightarrow CO + 3H_2 \tag{7}$$

$$C_xH_y + H_2O \rightarrow CO + H_2 \tag{8}$$

However, the cyclic stability of Ni-CaO catalyst needs to be improved to ensure the sustainability of H_2 production. Support materials with high surface area and mechanical strength such as Al_2O_3, ZrO_2, MgO, SiO_2, TiO_2, or La_2O_3 can be introduced into Ni-CaO catalyst to reduce sintering and deactivation of active sites on the catalyst [26–30]. However, this process may decrease CaO loading [31,32]. Nano-supported materials instead of conventional γ-Al_2O_3 or α-Al_2O_3 are vital (if needed) for increasing CaO loading. Wu and Wang [33] prepared a complex ZrO_2-Ni-nano-CaO catalyst by introducing Ni into composite support of nano-ZrO_2-$CaCO_3$ and Al_2O_3 (above 30 wt% of CaO loading) for stable H_2 production from steam methane reforming, creating an H_2 content of 97.3 vol% and kept above 80 vol% in 20 cyclic runs. Stonor et al. [34,35] proposed a two-step scheme involving the preparation of Ni/ZrO_2 catalyst and its mixing with $Ca(OH)_2$ sorbent, which is complex. Thereby, the direct incorporation of catalytic active metals (usually Ni) into CaO-based sorbents using chemical synthesis like sol–gel method is a promising approach as reported in references [20,33,36–41].

Although nickel has a favorable performance of tar cracking and reforming by breaking O–H and C–C bonds, low activity in water gas shift reaction, and may initiate methanation and coke deposition [42,43]. CeO_2, as a good inert material, can prevent the thermal sintering of metal particles owing to its high Tammann temperature of 1064 °C [44]. Zou et al. [45] found that CeO_2 not only improved the oxidizing ability of catalyst but also promoted oxidation of deposited carbon on the catalyst surface due to its outstanding redox behavior of rapidly reversible conversion of $Ce^{4+} \leftrightarrow Ce^{3+}$ for oxygen storing and releasing. The incorporation of CeO_2 for improving the catalytic activity and stability of Ni-CaO catalysts has been widely studied [36,39–41]. Particularly, Shokrollahi Yancheshmeh et al. [41] found that the NiO-CeO_2/$Ca_9Al_6O_{18}$-CaO exhibited excellent stability within 20 cycles with H_2 purity of 98%, H_2 yield of 91%, and CaO conversion of 97% in steam reforming of glycerol.

Most of these studies use bio-oil or its model compounds as feedstock for high H_2 purity and yield. Nevertheless, the gasification of real-world biomass is much more complicated than the steam reforming of oil model compounds or a simple gaseous mixture of CH_4, CO, or C_xH_y. There should be more carbon deposition and poisoning of the catalyst caused by larger-molecular tars and polluting volatiles from biomass. Besides, the application of CeO_2-modified Ni-CaO sorption bifunctional catalysts (CeO_2-Ni-CaO for short) in steam reforming of solid biomass is very limited in the open literature, to the best of our knowledge. In this study, we synthesized CeO_2-Ni-CaO catalysts for steam reforming of rice husk to hydrogen-rich gas in a two-stage system, aiming to improve the cyclic stability of the Ni-CaO catalyst on the basis of increasing the concentration and yield of H_2 compared to previous studies. The optimal Ce doping ratio (Ce/Ni molar ratio) and catalyst/biomass mass ratio were determined before evaluating the cyclic stability of catalysts. The differences and changes of physicochemical structure and carbon deposition of different catalysts were determined by various characterization techniques.

2. Materials and methods

2.1. Feedstock and catalyst

Rice husk was supplied as the biomass feedstock by Yihai (Taizhou) Grain and Oil Industry Co., Ltd., which was crushed and sieved into 0.075–0.150 mm sized powder, then dried in an oven at 105 °C for 8 h and sealed for storage. Properties of rice husk (air dried basis) are shown

Table 1

Composition, proximate, ultimate analyses, and calorific value of rice husk.

Composition (wt.%)			Proximate analysis (wt.%)[a]				Ultimate analysis (wt.%)					Q_{net} (MJ kg^{-1})[c]
Cellulose	Hemicellulose	Lignin	M	A	V	FC	C	H	N	S	O[b]	
44.07 (±0.24)	22.95 (±0.12)	25.75 (±0.14)	2.31 (±0.02)	10.55 (±0.10)	68.27 (±0.61)	18.87 (±0.18)	45.39 (±0.31)	5.24 (±0.05)	0.31 (±0.02)	0.20 (±0.01)	36.00 (±0.27)	16.60 (±0.08)

[a] M, moisture content; A, ash; V, volatile matters; FC, fixed carbon.

[b] Calculated by difference.

[c] Net calorific value at constant volume.

in Table 1.

CeO_2-Ni-CaO catalysts were prepared by a standard sol–gel method. All of the reagents (ACS reagent grade, ≥99%) for catalyst preparation were purchased from Macklin Co., Ltd. Specifically, 12.6 g of citric acid monohydrate ($C_6H_8O_7 \cdot H_2O$), 11.8 g of calcium nitrate tetrahydrate ($Ca(NO_3)_2 \cdot 4H_2O$), and 2.9 g of nickel nitrate hexahydrate ($Ni(NO_3)_2 \cdot 6H_2O$) were mixed into deionized water to obtain a homogeneous precursor solution (the molar ratios of citric acid, water, and Ca^{2+} to Ni^{2+} were 6:1, 200:1, and 5:1, respectively). Ce-doped catalysts were prepared by adding cerium nitrate hexahydrate ($Ce(NO_3)_3 \cdot 6H_2O$) into the precursor solution at Ce^{3+}/Ni^{2+} molar ratios of 0.25, 0.5, 0.7, and 1, respectively. Then, the mixture solution was stirred continuously at 80 °C until a translucent sol formed, the sol was subsequently dried at 120 °C overnight and formed a low-density foam gel and was thereupon crushed easily and calcined at 850 °C in a muffle furnace under air for 5 h at a heating rate of 5 °C min^{-1}. The obtained catalysts are denoted as Ni_1Ca_5, $Ce_{0.25}Ni_1Ca_5$, $Ce_{0.5}Ni_1Ca_5$, $Ce_{0.7}Ni_1Ca_5$, and $Ce_1Ni_1Ca_5$, respectively.

2.2. Experimental setup and procedure

The catalytic gasification of rice husk was carried out in a two-stage fixed-bed reactor system (Fig. 1) [25]. It mainly included a steam-feeding system with a precise syringe pump and steam generator, a vertical electric furnace with two separate heating stages (the actual height of the heating zone of each stage is 200 mm), a quartz tube as fixed-bed reactor (ID = 54 mm, H = 1150 mm), a condenser system, and followed by a gas cleaning, gas sampling, and measuring system.

According to the ideal reaction $C + H_2O + Ca(OH)_2 \rightarrow CaCO_3 + 2H_2$, the amount of $Ca(OH)_2$ at Ca/C molar ratio of 1 is theoretically sufficient for CO_2 sorption. Therefore, for each test, 1 g of rice husk was mixed evenly with 0.025–0.075 mm sized $Ca(OH)_2$ powder at Ca/C of 1:1. The biomass mixture sample supported by silica wool was loaded into a stainless-steel porous basket and hung at the top of the quartz tube 300 mm above the furnace, the steam-feeding tube was wrapped with 120 °C heating tapes to prevent condensation of steam. 15 mL (loose bulk volume) of the catalyst supported by silica wool was loaded into another basket closely fixed on the inner wall of the middle of the second stage. N_2 (99.999%) was supplied as a carrier gas to purge air in the reactor for 30 min at a flow rate of 200 mL min^{-1}. Then the two stages were both heated to 500 °C and kept for 40 min (the temperature was chosen based on our previous studies [25], where results indicated that the highest H_2 concentration was achieved at 500 °C in both stages). Simultaneously, a water flow of 0.17 g min^{-1} (S/C = 5) was fed into the steam generator by a syringe pump to produce steam and enter the reactor. When the desired temperature reached, the basket containing biomass sample was quickly pushed into the middle of the first stage and started timing and opening sampling bag inlet valve. The steam gasification of rice husk happened in the first stage and the derived intermediate gases passed through the catalyst bed and reformed in the second stage. Condensable liquid products (including tar and water) were captured in three condensers cooled by ice-water mixture, the non-condensable gases were cleaned using a glass fiber filter, dried by a bottle filled with allochroic silicagel, and collected in a gas sampling bag. The complete reaction time was determined by collecting the gas every two minutes and measured. The results showed that after 20 min of reaction, the main component of product gas was nitrogen, while the contents of other components were stable below 0.1 vol% and the reaction deemed complete. Thus, each experiment was performed for 20 min and the product gas was sampled for 20 min. To prevent the hydration of CaO in the catalyst into $Ca(OH)_2$ below 400 °C [16], the steam-feeding system was stopped immediately after 20 min and the reactor was continued at 500 °C and purged in N_2 flow for another 20 min to remove all the steam in the reactor. Each experimental condition was repeated at least three times and the results were expressed as the averages of replicated experiments and corresponding standard errors.

2.3. Products analysis

The gaseous products were analyzed offline with an Agilent 7890A gas chromatograph (GC) equipped with two thermal conductivity detectors (TCD) detecting H_2, CO, CO_2, N_2, and a flame ionization detector (FID) detecting CH_4 and C_2–C_3 hydrocarbons (C_2H_4, C_2H_6, C_3H_6, C_3H_8).

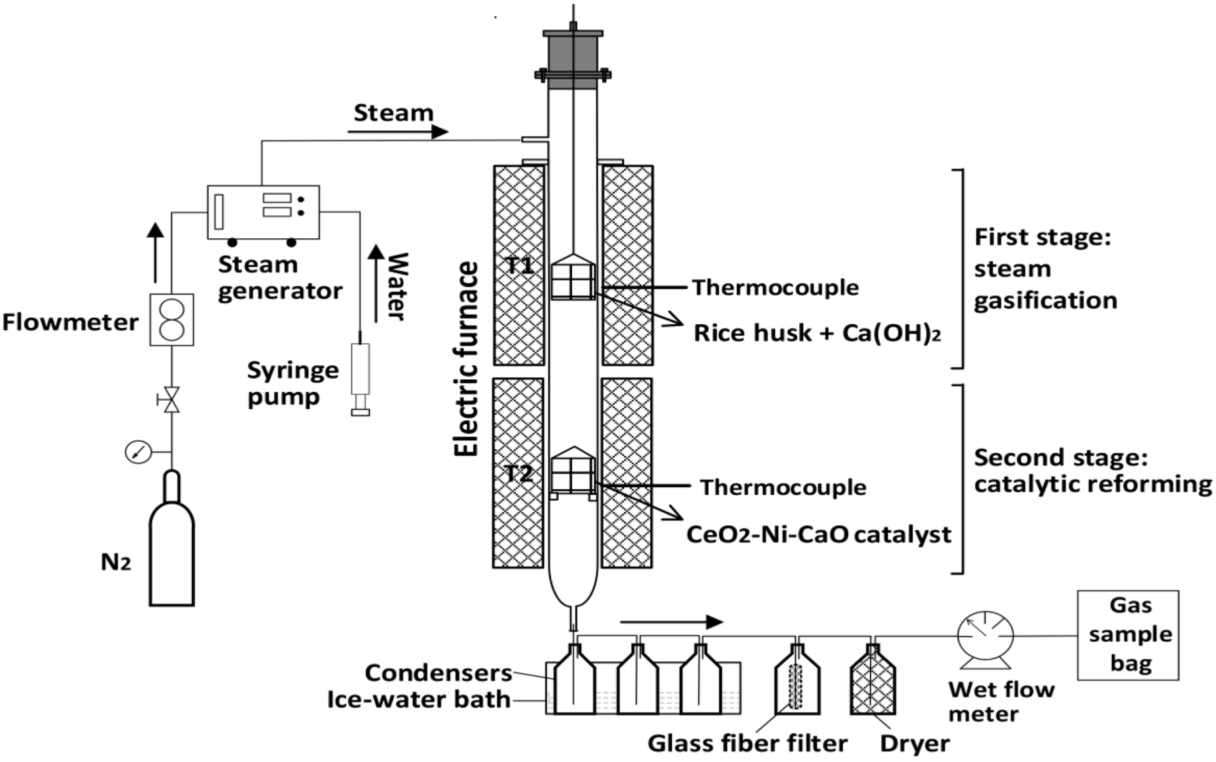

Fig. 1. Schematic diagram of experimental apparatus.

Standard gas was used to calibrate GC before analyzing the gas sample until the standard deviation is less than 0.5 vol%. Each gas sample was measured three times and averaged. Each gas yield was calculated by combining its concentration and the volume proportion of nitrogen with a constant flow rate at the condition of 1 atm and 25 °C. The yield of each gas was calculated as Eq. (9).

$$Y_g = \frac{V_{N_2}}{24.5 \times C_{N_2}} \times C_g \tag{9}$$

where Y_g is the yield of gas component, mmol $g^{-1}{}_{biomass}$; V_{N_2} is nitrogen volume, mL; C_g and C_{N_2} is the concentration of gas component and N_2 measured by GC, respectively, vol.%.

2.4. Catalyst characterizations

Fresh, used, and regenerated catalysts were collected and characterized. The surface morphologies of catalysts were observed using a Zeiss Sigma 300 scanning electron microscope (SEM) and a connected energy dispersive X-ray spectrometry (EDX) was used for the semi-quantitative analysis of elemental content. The microstructure of catalysts was further characterized by a JEOL JEM 200Plus high-resolution transmission electron microscopy (HRTEM) with a FEI talos F200S TEM for elemental mapping. Samples preparation for TEM analysis were dispersed evenly in ethanol with an ultrasonic device and pipetted on a carbon-coated copper grid.

The crystal phase of catalysts was determined by a PANalytical X'Pert PRO X-Ray Diffraction (XRD) with Cu Kα radiation ($\lambda = 1.5406$ Å) using a scanning step of 0.02° in the 10–90° 2θ range. The diffraction peaks were identified by X'Pert Highscore Plus software according to Joint Committee on Powder Diffraction Standards (JCPDS). The average crystal sizes (D_{hkl}) of compound species in catalysts were calculated by Scherrer equation (Eq. (10)) based on the main diffraction peaks.

$$D_{hkl} = \frac{K \cdot \lambda}{\beta \cdot cos\theta} \tag{10}$$

where D_{hkl} is crystal size, nm; K is dimensionless shape constant (0.89); λ is X-ray wavelength (0.15406 nm); β is full width at half the maximum intensity (FWHM) and θ is diffraction angle, °.

The actual metal loading concentration of fresh catalysts was measured with a PerkinElmer Optima 5300DV inductively coupled plasma optical emission spectrometer (ICP-OES). The pore properties of fresh catalysts were identified by N_2 adsorption–desorption method at −196 °C using a Quantachrome Autosorb-1 apparatus. The pore size distribution was obtained from the adsorption branch data via Barrett Joyner Halenda (BJH) method. The total pore volume (V_t) was measured at the P/P_0 of 0.95, and the micropore volume (V_m) was calculated by t-plot method. The specific surface area (S_{bet}) was determined with Brunauer Emmett Teller (BET) method, and $4V_t/S_{bet}$ was used to calculate the average pore diameter (D_p).

The chemical state of elements in fresh catalysts was determined by a Thermo Scientific K-Alpha X-ray photoelectronic spectrometry (XPS) with Al Kα radiation. The binding energies were calibrated with adventitious carbon C1s peak (284.8 eV). Peak fitting was conducted using Thermo Avantage software, and the content ratios of elements with different chemical states were estimated according to their deconvoluted peak areas of XPS spectra.

The quantitative analysis of carbon deposition of used catalysts was performed through thermogravimetry (TG) and derivative thermogravimetry (DTG) using a SwissMettler TGA/DSC3 + simultaneous thermal analyzer. TG test of each used catalyst (about 10 mg) was performed in the range of 50–850 °C under air and N_2 atmosphere (50 mL min^{-1}) at a 10 °C min^{-1} heating rate.

The functional groups and molecular structures of deposited carbon were determined using a Thermo Scientific Nicolet iS20 Fourier transform infrared spectrometer (FTIR) with a wave number scope of 400–4000 cm^{-1}. The deposited carbon species were identified by a Horiba evolution Raman spectrometry with a laser wavelength of 532 nm at a Raman shift of 50–3500 cm^{-1}.

3. Results and discussion

3.1. Characterization of the fresh catalysts

3.1.1. BET analysis

The pore characteristics of fresh catalysts are listed in Table 2, the N_2 adsorption–desorption isotherms and BJH pore size distributions of catalysts are shown in Fig. 2. According to the IUPAC classification [46], all catalysts display type-IV isotherms with type-H3 hysteresis loops, which is a typical characteristic of capillary condensation occurring in mesoporous due to the slit-shaped pores produced in the presence of citric acid. The N_2 adsorption capacity of catalysts increases with the increase of Ce doping. It should be noted that when the molar ratio of Ce to Ni increases to 1, the adsorption capacity is suddenly decreased, corresponding to the obvious decrease of the pore volume of $Ce_1Ni_1Ca_5$ catalyst, which is attributed to the penetration of Ce particles into the pores of CaO matrix which becomes the main contributor to surface area with the increase of CeO_2 content. In addition, the hysteresis loop moves toward a lower p/p_0 with the doping of Ce, implying that Ce plays an important role in generating more pores for catalyst [47]. The hollow snowflake-like structure of $Ce_{0.7}Ni_1Ca_5$ (Fig. 3d) is beneficial to form large pores, consequently creating the highest pore volume and surface area. Similar results of the pore properties of CeO_2-Ni-CaO catalysts were reported by Shokrollahi Yancheshmeh et al. [41]. The relatively higher average pore size and more mesopores formed by $Ce_{0.7}Ni_1Ca_5$ catalyst as confirmed by the pore size distribution in Fig. 2(b). The pore size distribution of $Ce_{0.7}Ni_1Ca_5$ catalyst is narrowest with the most intense peak corresponding to the most probable pore diameter of 3.09 nm, suggesting its uniform and abundant mesopores structure, which agrees well with its highest pore volume among all the catalysts. However, the micropore volume is decreased with the doping of Ce, which is resulted from the blockage of micropores caused by the increasing CeO_2 grains deposited on the catalyst surface. The metal atomic concentration of fresh catalysts was measured by ICP-OES and the results are listed in Table 2, it shows that the actual molar ratios of Ce to Ni in all catalysts are very close to the prescribed values.

3.1.2. SEM and TEM analyses

The surface morphology and elemental content of the fresh catalysts were characterized by SEM and EDX as shown in Fig. 3. All catalysts exhibit loose and porous structure, which is generated by the release of a large amount of heat and gas during the sol–gel preparation process [48]. A relatively smooth appearance of the Ni_1Ca_5 catalyst is observed, and with the doping of Ce, the appearance becomes rougher with smaller particles growing up on the cracked and fluffy substrate (Fig. 3b-e), resulting in higher pore volume and specific surface area as shown in Table 2, which would facilitate the effective inward diffusion of gas from the catalyst surface. Additionally, real metal loading of fresh catalysts

Table 2

Metal atomic concentration and pore properties of fresh catalysts.

Catalyst	Molar ratios[a]				Pore properties		
	Ni	Ce	Ca	S_{BET} (m^2 g^{-1})	V_t (cm^3 g^{-1})	V_m (cm^3 g^{-1})	D_P (nm)
Ni_1Ca_5	1	/	5.15	8.82	0.01170	0.00194	5.30
$Ce_{0.25}Ni_1Ca_5$	1	0.25	4.80	11.61	0.02058	0.00145	7.09
$Ce_{0.5}Ni_1Ca_5$	1	0.53	5.22	13.50	0.02668	0.00094	7.91
$Ce_{0.7}Ni_1Ca_5$	1	0.69	4.87	14.02	0.02726	0.00056	7.78
$Ce_1Ni_1Ca_5$	1	1.02	5.11	9.42	0.01358	0.00032	5.77

[a] Molar ratios normalized to Ni = 1 measured by ICP-OES.

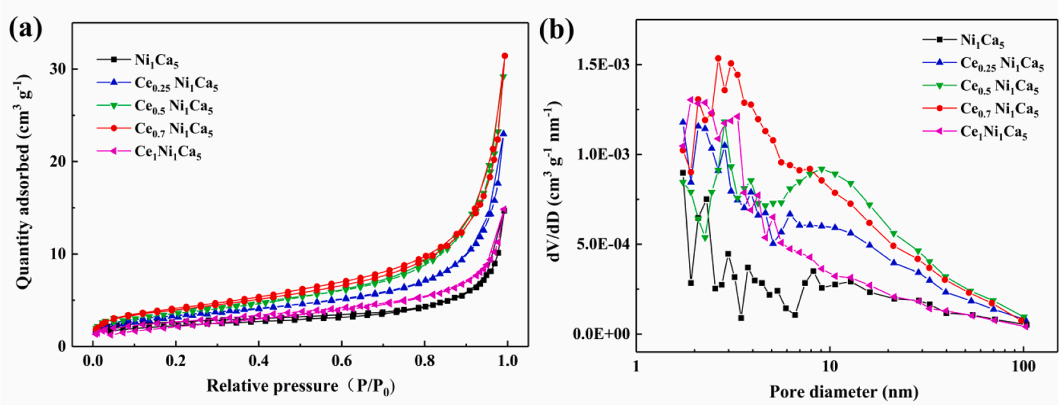

Fig. 2. N_2 adsorption–desorption isotherms (a) and pore size distributions (b) of fresh catalysts.

was semi-quantified by EDX, the actual loadings of Ni were 8.47–13.86 wt% and the maximum Ce loading was 20.58 wt%, indicating the successful introduction of Ce into catalysts in close accordance with the predetermined doping ratio.

TEM and HRTEM (Fig. 4a-e) provide further insight into the internal structure of catalysts. The obvious dark spots observed in the images are ascribed to Ni particles, and the lighter gray spots are attributed to Ce particles. Fig. 4a displays the irregular distribution of Ni particles on the CaO matrix. Interestingly, Ce-doped catalysts exhibit more uniform dispersion of metal particles with a dramatic decrease in the particle size (Fig. 4b-e) on the catalyst surface to transport gas molecules effectively [47]. The Ni particle distributions corresponding to the five TEM images were analyzed statistically by ImageJ software, and the results are shown in Fig. 4(f)-(j). All catalysts present a size distribution concentrated at 20–40 nm. However, Ni_1Ca_5 shows a broad size distribution with the largest average particle size of 70.07 nm. With the doping of Ce, the Ni particle distribution becomes narrow and more than 90 % of particles show a particle size of less than 70 nm, and the average particle size is decreased significantly by about 30%. Particularly, $Ce_{0.7}Ni_1Ca_5$ exhibits the narrowest particle size distribution and the smallest average particle size of 33.49 nm among all the catalysts, indicating its homogeneity with the smallest active metal size. The elemental mapping images of $Ce_{0.7}Ni_1Ca_5$ (Fig. 4k-o) also demonstrate that both Ce and Ni are uniformly dispersed throughout the catalyst and hardly any agglomeration can be seen. In addition, HRTEM images show that the increasingly obvious lattice fringes are observed with the doping of Ce, indicating the higher crystallinity of NiO and CeO_2. The lattice spacings of 2.09 Å and 3.12 Å represent the lattice planes of NiO (2 0 2) and CeO_2 (1 1 1) [47], respectively, which are assigned to the XRD peaks at around 43.2° and 28.5° respectively as shown in Fig. 5.

3.1.3. *XRD analysis*

XRD spectra of fresh catalysts are shown in Fig. 5. The results indicate the presence of NiO (cubic, JCPDS 96–432-0491) in each catalyst and CeO_2 (cubic, JCPDS 01–081-0792) in Ce-doped catalysts. The existence of $Ca(OH)_2$ (hexagonal, JCPDS 01–084-1271) in each catalyst is attributed to the hydration of CaO (cubic, JCPDS 96–900-6695) by moisture in the air during the cooling and storage process after calcination. It is worth noting that the CaO diffraction peaks disappear in all Ce-doped catalysts (except $Ce_1Ni_1Ca_5$), which is related to the effective diffusion of water molecules into the catalyst to react with CaO due to the fluffy and porous structure and higher pore volume (Table 2) of Ce-doped catalysts compared to Ni_1Ca_5 catalyst. $Ce_1Ni_1Ca_5$, which should be noted, both contains CaO and $Ca(OH)_2$ species, which is ascribed to the gradual growth of CeO_2 grains with the increase of Ce doping ratio until the crystal size of CeO_2 in $Ce_1Ni_1Ca_5$ significantly exceeds that of NiO as shown in Table 3, resulting in a wide range of pore blockage and hindering the diffusion of water molecules, so CaO cannot be completely converted to $Ca(OH)_2$ at higher doping ratio of Ce. Overall, the crystal size of NiO is decreased by the incorporation of Ce, which is attributed to the inhibition of metal sintering by the interaction between CeO_2 and NiO, as reported by Roh et al [49].

3.1.4. *XPS analysis*

XPS analysis for fresh catalysts is performed to identify chemical states. The XPS spectra of Ni2p (Fig. 6a) are fitted as two spin–orbit dipoles of NiO and $Ni(OH)_2$ as well as two vibration satellite peaks using the Gaussian fitting method [50]. In the Ni2p spectrum, peaks located at 853.7 eV and 871.6 eV of the binding energies are ascribed to NiO, and peaks at 855.6 eV and 873.3 eV of the binding energies are assigned to $Ni(OH)_2$ [51], accompanied by two satellite peaks at higher binding energies of 861.0 eV and 879.3 eV, respectively [47]. Ce3d spectra are more complicated because of the co-existence of two different cerium valence states [52]. As shown in Fig. 6(b), Ce3d is composed of 10 feature peaks grouped as V (Ce^{4+}) and U (Ce^{3+}). Peaks denoted as V_0, V_1, V_2, U_1, U_0 are assigned to $3d_{5/2}$ spin–orbit split doublet, and the other peaks marked as V_0', V_1', V_2', U_1', U_0' corresponded to $3d_{3/2}$ spin–orbit split doublet [53,54]. The binding energy values are, respectively, 881.6 eV (V_0), 888.3 eV (V_1), 897.4 eV (V_2), 879.2 eV (U_1), 884.0 eV (U_0), 900.2 eV (V_0'), 907.1 eV (V_1'), 915.9 eV (V_2'), 899.5 eV (U_1'), 902.2 eV (U_0'). Thereby, Ce in the catalyst mainly exists in the valence state of 4+ and 3+, and the ratio of Ce^{4+} to Ce^{3+} decreases with the doping of Ce as shown in Table 4, suggesting that more oxygen vacancies are generated by Ce^{3+} with the doping of Ce. On the other hand, the ratio of NiO to $Ni(OH)_2$ is increased with the doping of Ce and reached the highest value in $Ce_{0.7}Ni_1Ca_5$, indicating that the addition of Ce species enhances the stability of Ni^{2+} in the form of more oxides than hydroxides. Besides, Fig. 6(c) shows a separation of 3.5 eV in the binding energies and an intensity ratio of 1/2 in the peaks of $Ca2p_{3/2}$ and $Ca2p_{1/2}$, confirming the existence of Ca^{2+} [55]. Fig. 6(d) shows three main peaks (donated as O_1, O_2, and O_3) exist in the O1s spectrum, corresponding to the metal oxide (O_1, 528.8 eV), oxygen ions (O_2, 531.4 eV), and metal hydroxide or physicochemical adsorbed water on the surface of catalysts (O_3, 533.0 eV) [56]. Based on the above analyses, the fresh catalysts contain components composed of Ce^{4+}, Ce^{3+}, Ni^{2+}, Ca^{2+}, and O^{2-}.

3.2. *Effect of Ce doping ratio on gas components and yields*

The effect of Ce doping ratio on gas component concentration and yield was investigated under a condition of 500 °C, S/C = 5 (mol/mol), and catalyst/biomass = 2.5 (g/g). The results are shown in Fig. 7. Compared with Ni_1Ca_5 catalyst, the H_2 concentration was increased by $Ce_{0.7}Ni_1Ca_5$ catalysts from 79.54(±0.48) to 85.81(±0.39) vol.%, and H_2 yield was increased from 28.20(±0.37) to 35.82(±0.28) mmol $g^{-1}_{biomass}$. The contents of CO and CH_4 are decreased with a slight increase of the

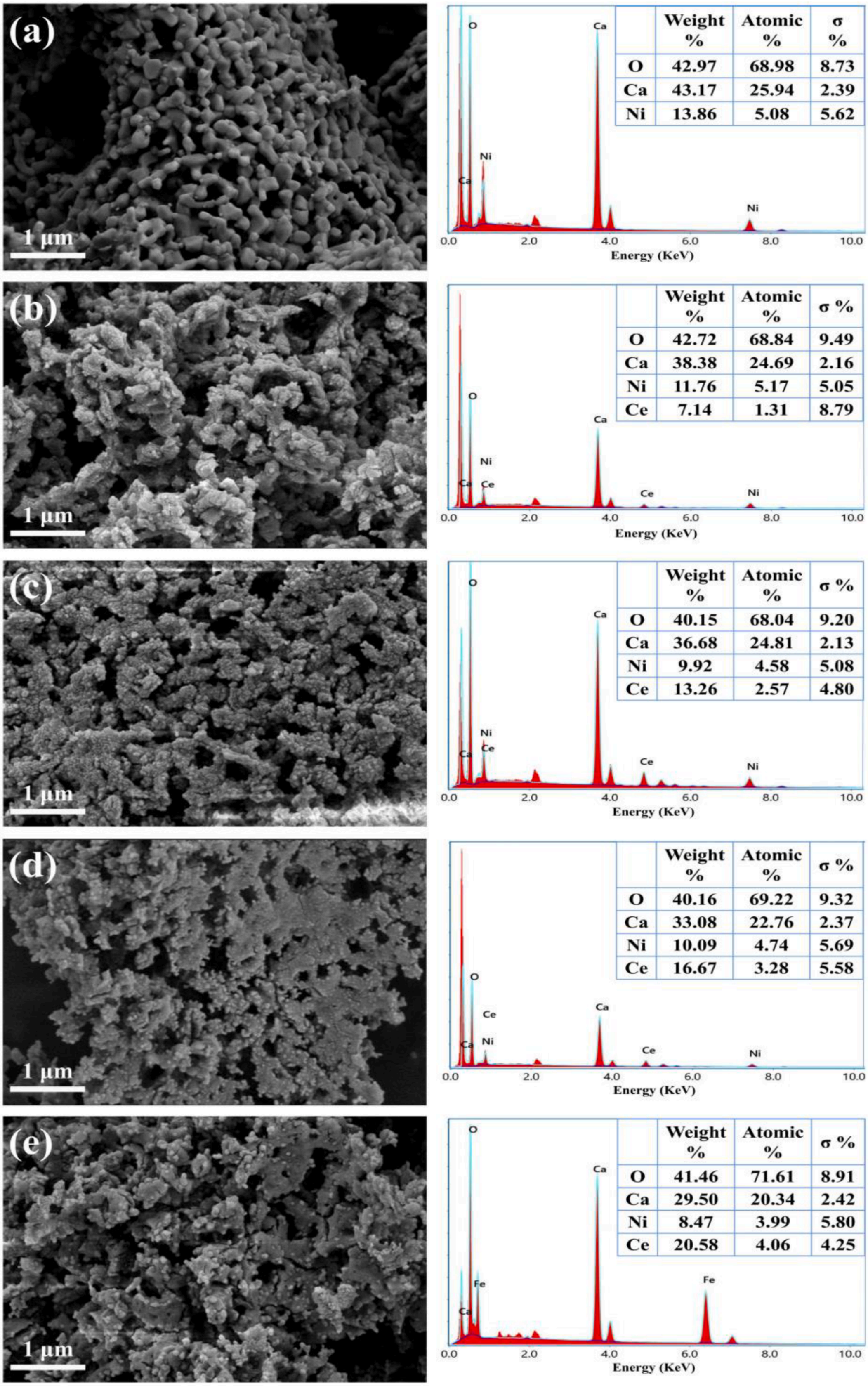

(a)

	Weight %	Atomic %	σ %
O	42.97	68.98	8.73
Ca	43.17	25.94	2.39
Ni	13.86	5.08	5.62

(b)

	Weight %	Atomic %	σ %
O	42.72	68.84	9.49
Ca	38.38	24.69	2.16
Ni	11.76	5.17	5.05
Ce	7.14	1.31	8.79

(c)

	Weight %	Atomic %	σ %
O	40.15	68.04	9.20
Ca	36.68	24.81	2.13
Ni	9.92	4.58	5.08
Ce	13.26	2.57	4.80

(d)

	Weight %	Atomic %	σ %
O	40.16	69.22	9.32
Ca	33.08	22.76	2.37
Ni	10.09	4.74	5.69
Ce	16.67	3.28	5.58

(e)

	Weight %	Atomic %	σ %
O	41.46	71.61	8.91
Ca	29.50	20.34	2.42
Ni	8.47	3.99	5.80
Ce	20.58	4.06	4.25

Fig. 3. SEM-EDX results of fresh catalysts Ni_1Ca_5 (a), $Ce_{0.25}Ni_1Ca_5$ (b), $Ce_{0.5}Ni_1Ca_5$ (c), $Ce_{0.7}Ni_1Ca_5$ (d), $Ce_1Ni_1Ca_5$ (e).

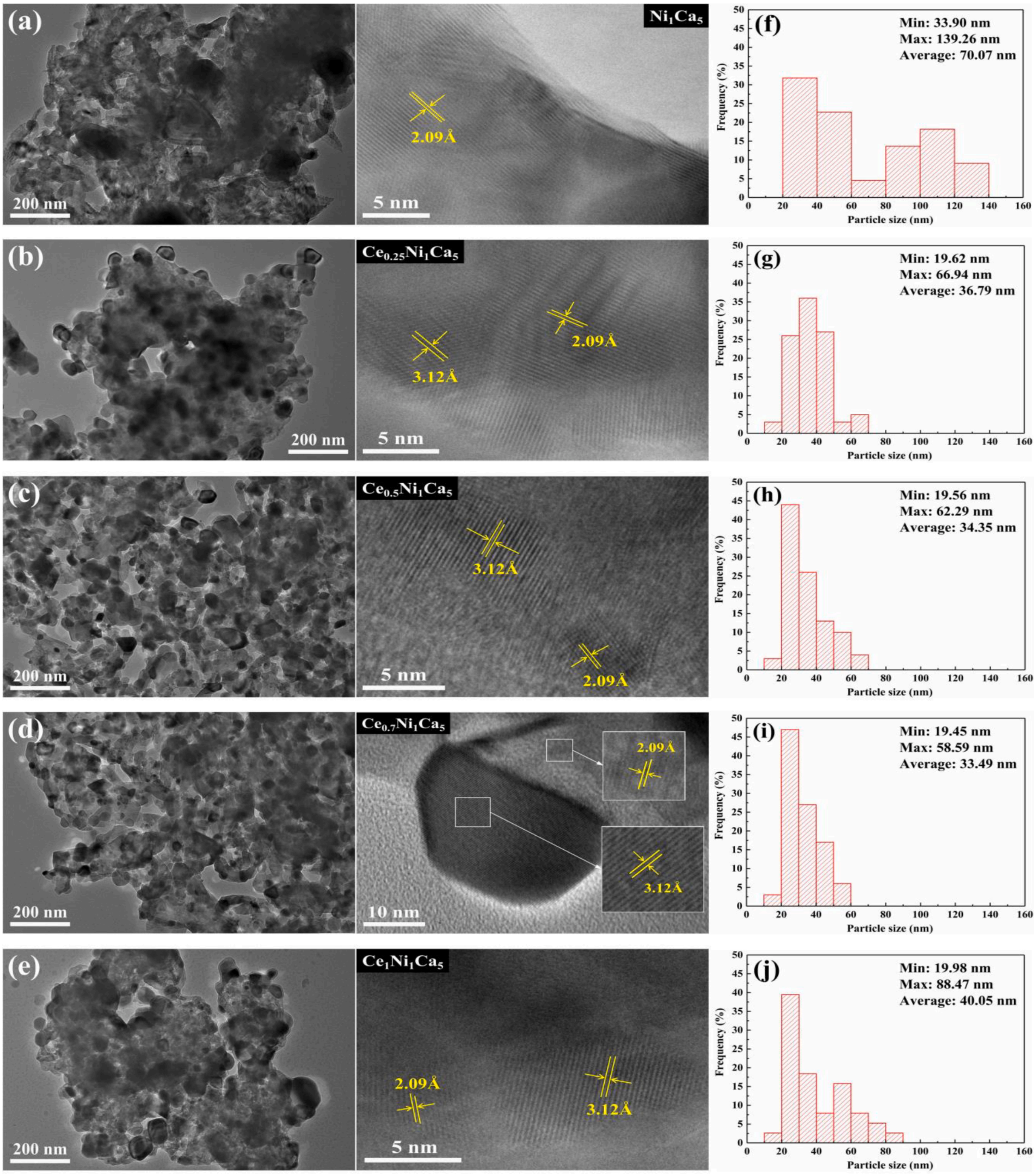

Fig. 4. TEM, HRTEM images of fresh catalysts Ni_1Ca_5 (a), $Ce_{0.25}Ni_1Ca_5$ (b), $Ce_{0.5}Ni_1Ca_5$ (c), $Ce_{0.7}Ni_1Ca_5$ (d), $Ce_1Ni_1Ca_5$ (e), and the corresponding Ni particle size distributions (f)-(j), and elemental mappings (k)-(o) of $Ce_{0.7}Ni_1Ca_5$.

content of C_2-C_3 hydrocarbons with the doping of Ce, it can be concluded that the steam reforming of CO and CH_4 rather than hydrocarbons are moderately enhanced with the doping of Ce, which means that CeO_2 can promote WGS (Eq. (6)) and steam methane reforming (SMR, Eq. (7)) in some extent, as widely reported by previous studies [26,57–59].

A model of redox reaction mechanism over the CeO_2-Ni-CaO catalysts is proposed as shown in Fig. 8. The first step involves rapid reduction of Ni^{2+} to Ni by adsorbed H_2, CO, CH_4, and C_xH_y hydrocarbons, along with the formation of H_2O and CO_2 (Eq. (11)), meanwhile, the adsorbed H_2 extracts lattice oxygen from CeO_2 to form H_2O (Eq. (12)), resulting in the reduction of oxidized ceria (Ce^{4+}) to reduced ceria (Ce^{3+}) with the appearance of oxygen vacancies. The second step involves the reduction of H_2O by Ni active sites to produce H_2 and Ni becomes Ni^{2+} (Eq. (13)). Simultaneously, the interaction of H_2O over oxygen vacancy leads to the oxidation of Ce^{3+} to Ce^{4+} and more release of H_2 (Eq. (14)). In addition, Ni displays strong interaction with Ce that more Ni cations with smaller formal charge occupy the lattice positions of Ce cations, showing the nearest-neighbor coordination of Ni-O embedded into ceria lattice [58], which induces the creation of more oxygen vacancies that facilitate the fracture of O–H bonds of water [60]. Ni-O-Ce interactions also produce interfacial active sites to break C–H

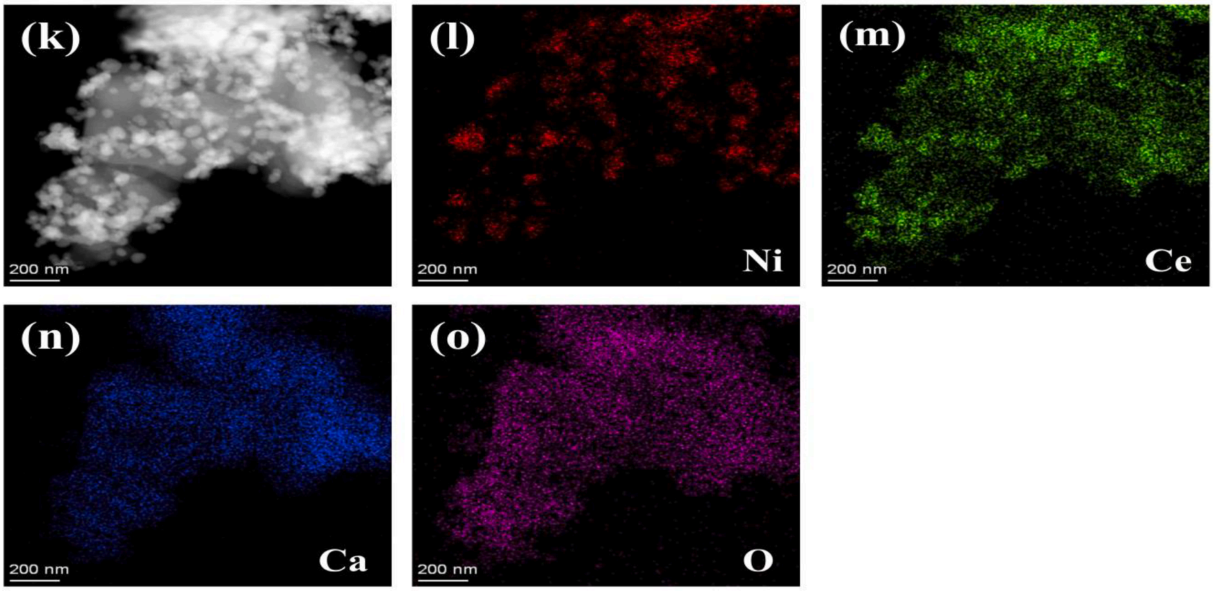

Fig. 4. (*continued*).

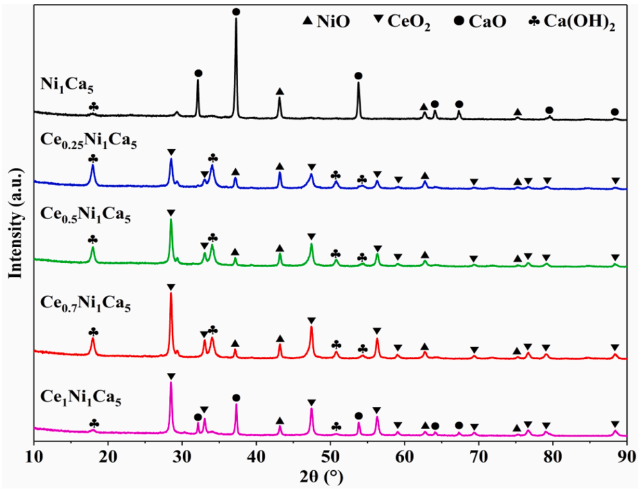

Fig. 5. XRD spectra of the fresh catalysts.

and C–C bonds for the subsequent formation of H_2 and CO_2 [60]. A similar redox process has been reported by previous studies [47,61–63]. Finally, the released oxygen from oxidized ceria reacts with the possible deposited carbon on the catalyst to form CO_2, which was immediately captured in situ by CaO into $CaCO_3$.

$$Ni^{2+} + H_2/CO/CH_4/C_xH_y \leftrightarrow Ni + H_2O + CO_2 \quad (11)$$

$$Ce^{4+} + H_2 \leftrightarrow H_2O + Ce^{3+} \quad (12)$$

$$Ni + H_2O \leftrightarrow Ni^{2+} + H_2 \quad (13)$$

$$Ce^{3+} + H_2O \leftrightarrow H_2 + Ce^{4+} \quad (14)$$

In addition, the ratio of Ce to Ni reveals the degree of WGS and SMR reactions. The concentration and yield of H_2 are both increased with the Ce doping ratio but decreased at the Ce doping ratio of 1, and other gas contents are increased accordingly, which is due to the considerable decrease of pore volume (Table 2) at the Ce doping ratio of 1, most of the mesoporous are blocked by the increasing CeO_2 grains deposited on the catalyst surface and gases are hardly diffused inward to the catalyst, resulting in a higher CO_2 yield of $Ce_1Ni_1Ca_5$. Among all the catalysts, $Ce_{0.7}Ni_1Ca_5$ exhibits the highest activity with an H_2 concentration of 85.81(±0.39) vol.% and H_2 yield of 35.82(±0.28) mmol $g^{-1}_{biomass}$, producing the lowest content of CO_2 (3.62(±0.16) vol.%), CO (4.27 (±0.11) vol.%), CH_4 (4.49(±0.18) vol.%), and C_2-C_3 (1.81(±0.09) vol. %), correspondingly, which is related to its highest pore volume for promoting WGS and SMR reactions to produce more H_2. The performance is much better than that reported by Waheed and Williams [38] (H_2 concentration and yield are 59.13 vol% and 25.44 mmol $g^{-1}_{biomass}$, respectively at 950 °C with Ni-dolomite catalyst) and Wu et al. [37] (H_2 concentration and yield are 55.0 vol% and 22.2 mmol $g^{-1}_{biomass}$, respectively at 800 °C with Ni-Ca-Al catalyst). Detailed comparisons of hydrogen production results with previous studies are summarized in Table 5.

XRD spectra of the used catalysts are presented in Fig. 9, and the

Table 3
Average crystal size of fresh and used catalysts from XRD results.

Catalyst	Average crystal size (nm)							
	Fresh catalysts[a]				Used catalysts[b]			
	NiO	CeO_2	CaO	$Ca(OH)_2$	NiO	Ni	CeO_2	$CaCO_3$
Ni_1Ca_5	25.14	/	24.68	4.14	22.00	17.68	/	28.20
$Ce_{0.25}Ni_1Ca_5$	17.60	10.55	/	11.84	14.67	14.73	12.06	16.92
$Ce_{0.5}Ni_1Ca_5$	16.00	14.07	/	9.21	14.66	12.63	18.76	18.80
$Ce_{0.7}Ni_1Ca_5$	12.57	21.11	/	9.20	12.57	9.82	28.14	21.17
$Ce_1Ni_1Ca_5$	17.60	24.12	17.27	5.18	19.55	17.68	28.76	24.17

[a] Calculated by Scherrer equation based on the diffraction peaks in Fig. 5 at 2θ around 43.2° (NiO), 28.5° (CeO_2), 37.3° (CaO), and 17.9° ($Ca(OH)_2$), respectively.
[b] Calculated by Scherrer equation based on the diffraction peaks in Fig. 9 at 2θ around 43.2° (NiO), 44.4° (Ni), 28.5° (CeO_2), and 29.3° ($CaCO_3$), respectively.

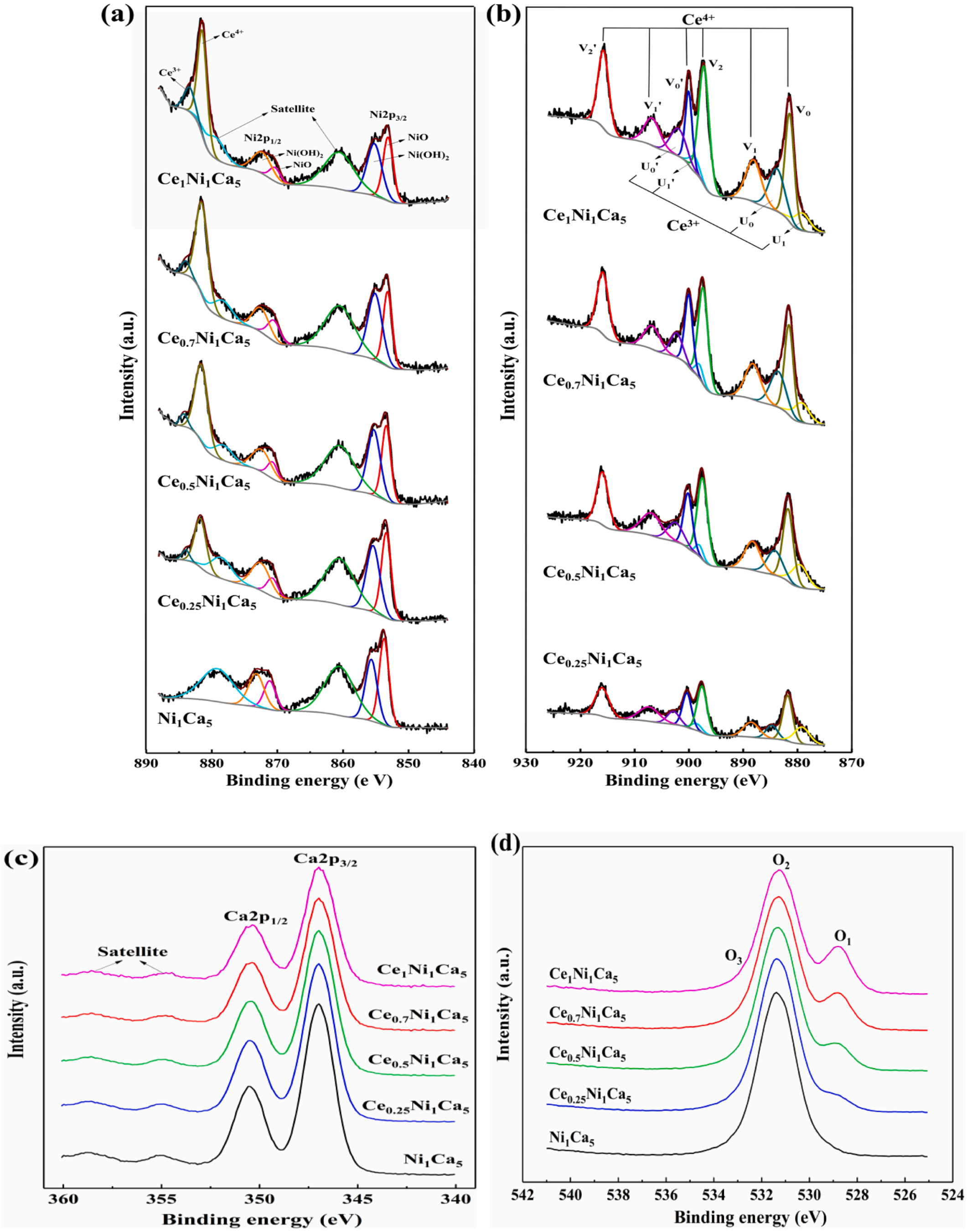

Fig. 6. XPS spectra for Ni2p (a), Ce3d (b), Ca2p (c), and O1s (d) of fresh catalysts.

Table 4
XPS area ratio of chemical states of Ni and Ce species for fresh catalyst.

	Ni_1Ca_5	$Ce_{0.25}Ni_1Ca_5$	$Ce_{0.5}Ni_1Ca_5$	$Ce_{0.7}Ni_1Ca_5$	$Ce_1Ni_1Ca_5$
NiO:Ni $(OH)_2$	1.143	1.284	1.344	1.349	1.200
Ce^{4+}:Ce^{3+}	/	3.267	3.182	3.076	3.068

average crystal size of used catalysts are listed in Table 3. Peaks of Ni (cubic, JCPDS 96–432-0493), NiO, $CaCO_3$ (rhombohedral, JCPDS 01–072-1937) are observed and no CaO peaks exist in all used catalysts, suggesting that the complete carbonation of CaO by CO_2 and majority reduction of NiO by reducing gases produced from biomass gasification. Under 500 °C, only the surface of shell NiO is reduced while bulk NiO is difficult to be reduced due to its higher reduction temperatures (500–600 °C) [65], which was also observed in our previous studies [25]. Therefore, NiO is not completely reduced to Ni on all used catalysts but shows a lower crystal size of NiO after being reduced, and the crystal size of NiO and Ni of used catalysts was also decreased with the Ce doping ratio but occurs slight sintering of NiO and Ni species for $Ce_1Ni_1Ca_5$. CeO_2 always exists in the used Ce-doped catalysts reacted at 500 °C because of the higher reduction temperature of CeO_2 to CeO_{2-x} (above 780 °C) [45,66]. CeO_2 crystal size in each used catalyst is larger than that of fresh catalysts and the $CaCO_3$ crystal size also increases with the Ce doping ratio, which is associated with agglomeration or partial sintering of $CaCO_3$ with the increase of CeO_2 crystal size. It can be verified by the SEM images (Fig. 10) that display the growth and agglomeration of metal particles in the used catalysts, resulting in the

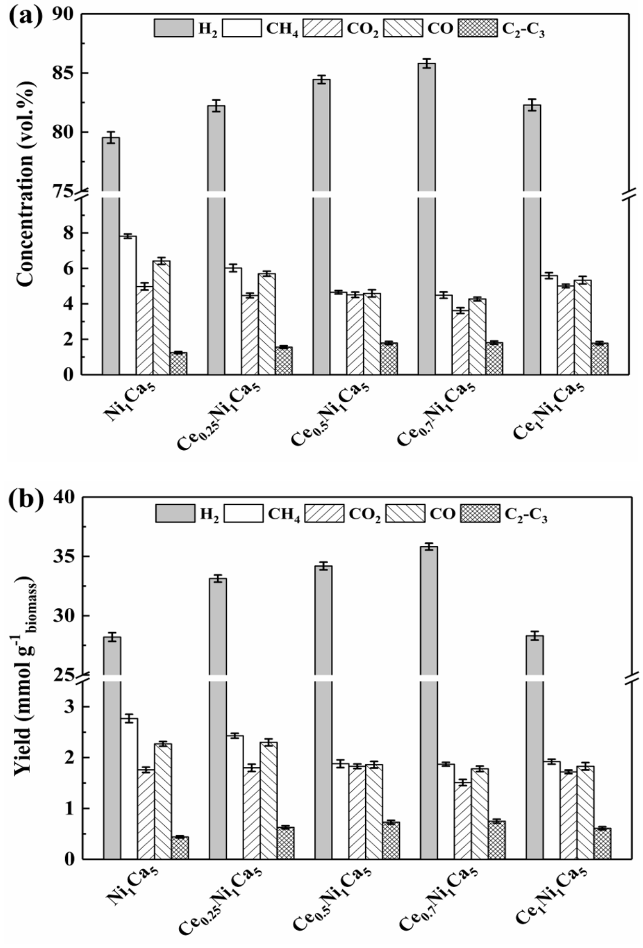

Fig. 7. Gas component concentration (a) and yield (b) under different catalysts.

pore blockage and forming a denser morphology compared with fresh catalysts.

Fig. 11 provides the TG and DTG thermograms of the used catalysts. In air atmosphere, a slight mass gain at a lower temperature of 300–400 °C is associated with the oxidation of metallic Ni to NiO, followed by a slight mass loss linked to the oxidation of amorphous carbon deposited on the catalyst surface at the range of 400–550 °C [29]. Since the oxidation temperature of amorphous carbon is lower than that of filamentous carbon [32,39], the dramatically mass loss at a higher temperature of 550–800 °C is related to the decomposition of $CaCO_3$ accompanied by oxidation of deposited filamentous carbon. The amount of $CaCO_3$ was determined as the mass loss measured in N_2 atmosphere at the stage of 575–800 °C. Then the amount of deposited carbon was calculated by subtracting the amount of $CaCO_3$ from the total mass loss measured in air, the results were summarized in Table 6. The carbon deposition of Ce-doped catalysts is less than 35% that of Ni_1Ca_5 and continues to decline with the Ce doping ratio, which is ascribed to the oxidation of carbon in the presence of CeO_2 with high oxidizing ability. The decrease of $CaCO_3$ with the doping of Ce is due to that more CaO covered by increasing CeO_2 grains cannot be carbonated to $CaCO_3$. However, the weight loss peak temperature of $CaCO_3$ decomposition moves toward higher values with the doping of Ce, indicating more stable $CaCO_3$ formed and improving CO_2 sorption stability. It can be concluded that the incorporation of CeO_2 into the catalyst not only improves the resistance to carbon deposition but also stabilizes CO_2 sorption.

3.3. Effect of catalyst/biomass mass ratio on H_2 yield

$Ce_{0.7}Ni_1Ca_5$ catalyst that exhibits the best performance in H_2 production was used for the test of rice husk gasification in catalyst/biomass ratios of 1.5, 2, 2.5, and 3.0. The effect of catalyst/biomass ratio on product gas concentration and H_2 yield is shown in Fig. 12. The H_2 concentration increases steadily from 82.14(±0.49) to 85.81(±0.39) vol.% and remains stable at catalyst/biomass ratios of 2.5, accompanied by a decrease of other components, indicating that the increase of catalyst/biomass ratio increases the reaction residence time for steam reforming of derived gases into H_2. Although enhanced steam reforming of CH_4 and C_2-C_3 will aggravate the formation of CO, which is consistent with the higher CO content at catalyst/biomass of 3, fortunately, H_2 yield increases dramatically from 26.63(±0.23) to 35.82(±0.28) mmol $g^{-1}_{biomass}$ when catalyst/biomass ratio increases from 2 to 2.5 and reaches the maximum at 2.5, indicating that catalyst/biomass ratio of 2.5 provides enough residence time for derived gases to produce H_2. Considering that increasing catalyst loading will increase the catalytic cost. Thus, the optimal catalyst/biomass mass ratio is 2.5 in this study.

3.4. Recyclability of $Ce_{0.7}Ni_1Ca_5$ catalyst for H_2 production

To investigate the recyclability and stability of $Ce_{0.7}Ni_1Ca_5$ catalyst, the cyclic test was carried out under a condition of 500 °C, S/C = 5 (mol/mol), and catalyst/biomass = 2.5 (g/g). After each experiment, the used catalyst was calcined at the same reactor for regeneration at 850 °C for 20 min in airflow of 500 mL min^{-1} for the oxidation of deposited coke and metallic nickel as well as decomposition of $CaCO_3$. Then, the fresh biomass mixture was introduced in the gasification stage. This cycle involves the redox reaction of NiO (Eq. (11)) and reversible carbonation-

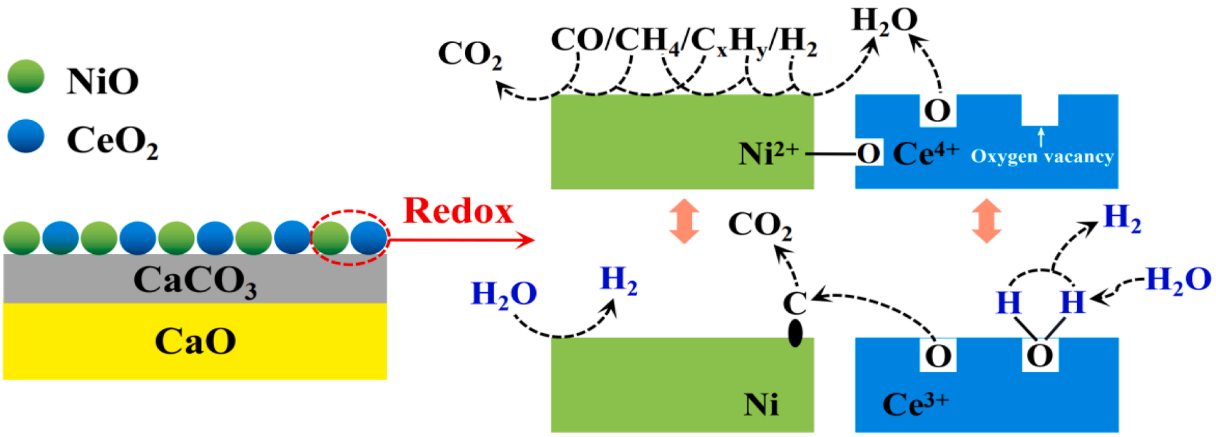

Fig. 8. Redox reaction mechanism over CeO_2-Ni-CaO catalysts.

Table 5
Comparisons of hydrogen production results with previous studies.

Feedstock	Catalyst	Synthesis method	Reaction condition[a]	Regeneration condition	Maximum H_2 concentration/yield	Reaction time	Ref.
Rice husk	$Ce_{0.7}Ni_1Ca_5$	Sol-gel	500 °C, S/C = 5	850 °C for 20 min in air	85.81 vol% / 35.82 mmol $g^{-1}_{biomass}$	Unchanged (10 cycles)	This study
Rice husk	10% Ni-dolomite	Wet impregnation	950 °C, S/B = 1.37		59.13 vol% / 25.44 mmol $g^{-1}_{biomass}$		[38]
Cellulose	20%Ni-Ca-Al	Coprecipitation	500 °C (pyrolysis), 800 °C (catalysis), S/B = 2		55 vol% / 22.2 mmol $g^{-1}_{biomass}$		[37]
Rice husk	nano-NiO/ γ-Al_2O_3	Deposition-precipitation	800 °C (gasification), 900 °C (catalysis), 800 °C, S/B = 1.33, ER = 0.22		48.7 vol%		[64]
Biogas	Ni-Ce/CaO	Wet mixing	600 °C, S/C = 3:1	850 °C for 30 min in N_2	85 mol.%	Unchanged (5 cycles)	[40]
Toluene	10%Ni/Ca-Al-Ce (0.2)	Coprecipitation	650 °C, S/C = 3.4 WHSV = 13.8 L·$(h{\cdot}g_{cat})^{-1}$		64 mol.%	Unchanged (800 min)	[39]
Glycerol	20%Ni-15%CaO/ γ-Al_2O_3	Wet impregnation	500 °C, S/C = 5.4, GHSV = 200000 h^{-1}		65 mol.% / 35 mol.%	Unchanged (30 h)	[32]
Tar model	10%Ni/ dolomite/La_2O_3	Coprecipitation	700 °C, S/C = 1, WHSV = 20 L·$(h{\cdot}g_{cat})^{-1}$		52 mol.% / 66.2 mol.%	Unchanged (300 min)	[29]

[a] S/B, steam/biomass molar ratio; S/C, steam/carbon molar ratio; WHSV, weight hourly space velocity; GHSV, Gas hourly space velocity; ER, air equivalence ratio.

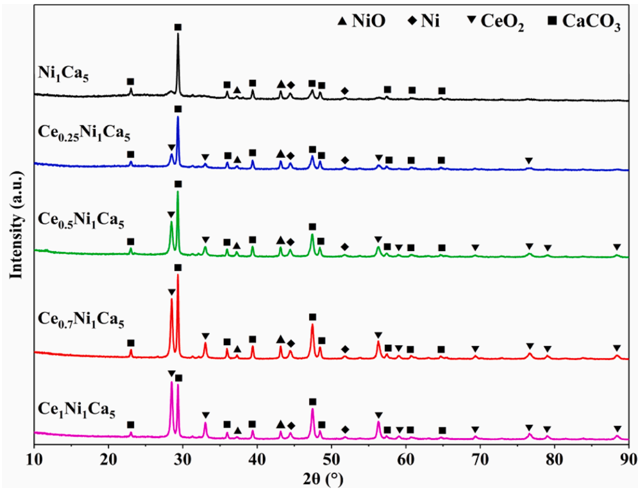

Fig. 9. XRD spectra of the used catalysts.

calcination of CaO (Eq. (3)).

Changes in H_2 yield and gas distribution with cycle time are presented in Fig. 13. For Ni_1Ca_5 catalyst, the H_2 yield and H_2 concentration decrease with the increasing cycle time and keep stable at the 7th time. The maximum declines of H_2 concentration and H_2 yield are 13.65% and 46.31%, respectively. Compared with Ni_1Ca_5 catalyst, the decay rate of H_2 concentration of $Ce_{0.7}Ni_1Ca_5$ catalyst becomes gentle, and H_2 concentration remains above 81.88 vol% after 10 cycles and the maximum decline of H_2 concentration is only 4.58%, which is only about 34% that of Ni_1Ca_5 catalyst. Significantly, H_2 yield is unexpectedly increased to 38.61 mmol g^{-1} by $Ce_{0.7}Ni_1Ca_5$ at the second time, it seems that the catalytic activity of the catalyst becomes better due to the significant decrease of CeO_2 crystal size in the regenerated catalyst after the first use and even lower than that of the fresh catalyst (as shown in Table 3 and Table 7), exposing more CaO covered by CeO_2 grains and adsorbing more CO_2 to promote WGS reaction to produce H_2. It was not until the $Ce_{0.7}Ni_1Ca_5$ was used for 5 cycles that the H_2 yield began to be lower than that obtained at the first time, the decline rate increases slightly after 6 cycles but remains stable after 7 cycles. The lowest H_2 yield of 32.11 mmol g^{-1} is achieved by $Ce_{0.7}Ni_1Ca_5$, which is more than twice that achieved by Ni_1Ca_5 (15.14 mmol g^{-1}). In addition, the decrease of CH_4 but an increase of CO_2, CO, and C_2–C_3 contents with the cycle time of $Ce_{0.7}Ni_1Ca_5$ is much lower than that of Ni_1Ca_5, which slows down the

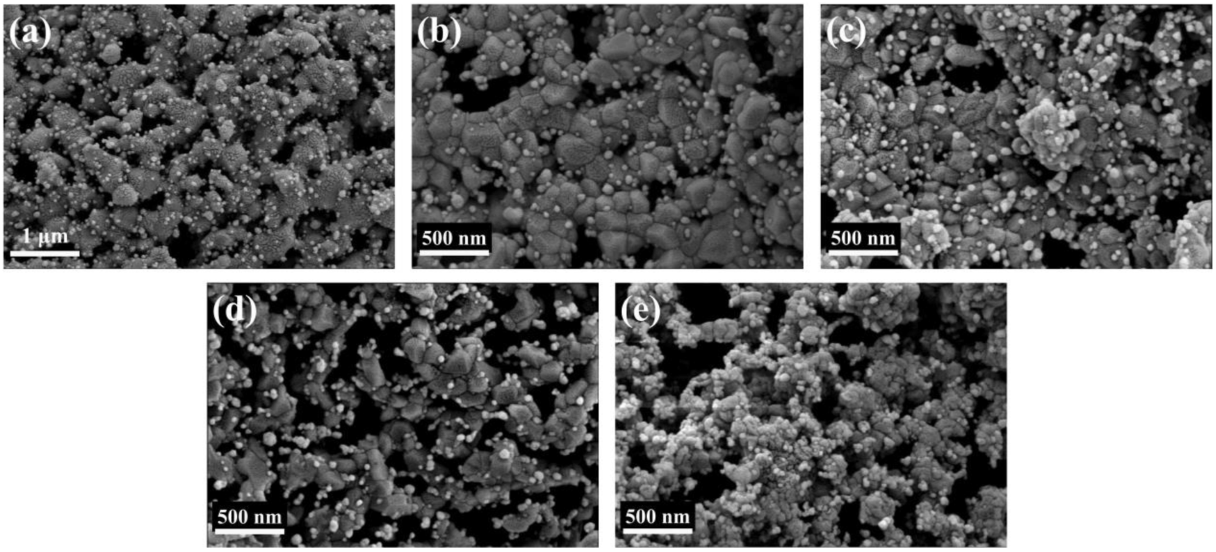

Fig. 10. SEM images of the used catalysts Ni_1Ca_5 (a), $Ce_{0.25}Ni_1Ca_5$ (b), $Ce_{0.5}Ni_1Ca_5$ (c), $Ce_{0.7}Ni_1Ca_5$ (d), $Ce_1Ni_1Ca_5$ (e).

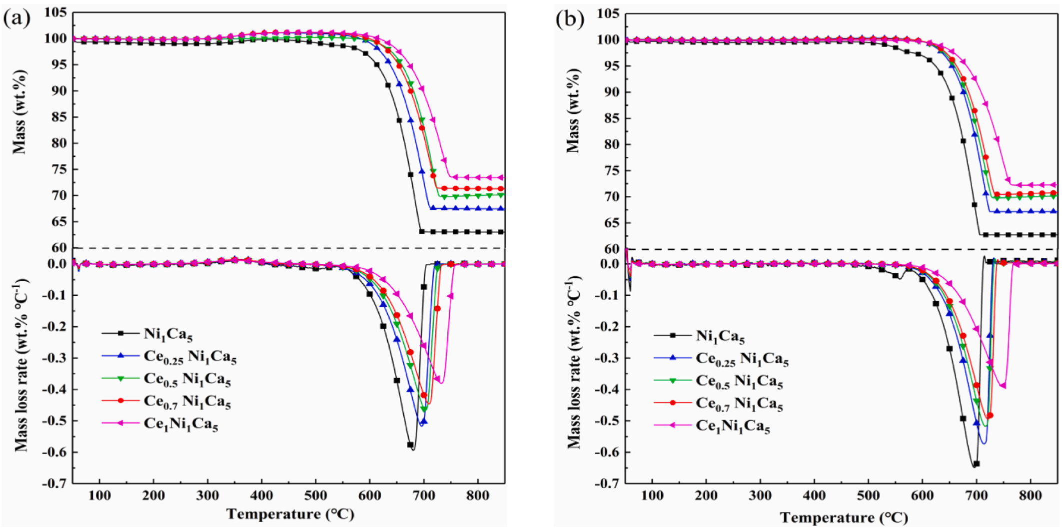

Fig. 11. TG and DTG thermograms of the used catalysts in air atmosphere (a) and N_2 atmosphere (b).

Table 6
Amount of deposited carbon and $CaCO_3$ of the used catalysts.

	Ni_1Ca_5	$Ce_{0.25}Ni_1Ca_5$	$Ce_{0.5}Ni_1Ca_5$	$Ce_{0.7}Ni_1Ca_5$	$Ce_1Ni_1Ca_5$
Deposited carbon (mg $g^{-1}_{catalyst}$)	21.13	7.35	6.81	6.01	2.75
$CaCO_3$ (mg $g^{-1}_{catalyst}$)	349.59	329.03	298.27	292.72	275.03

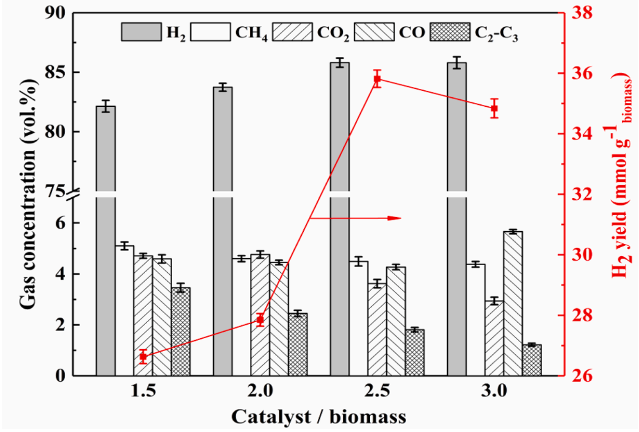

Fig. 12. Effect of catalyst/biomass mass ratio on product gas distribution and H_2 yield.

decline of the concentration and yield of H_2, maintaining a stable catalytic activity in H_2 production.

The cyclic stability of $Ce_{0.7}Ni_1Ca_5$ is relatively better than that reported by Phromprasit et al. [40] (a stable H_2 purity of 85 mol.% during 5 cycles but 63 mol.% in the post-breakthrough period, at 600 °C with Ni-Ce/CaO catalyst for steam reforming of biogas) as shown in Table 5. It is found that compared with the conventional catalytic steam reforming of biogas or tar modals, the catalytic gasification of real solid biomass with $Ce_{0.7}Ni_1Ca_5$ catalyst in this study exhibits a remarkable H_2 production and favorable cyclic stability.

XRD spectra of the first regenerated catalysts and used catalysts after the 5th and 10th time are presented in Fig. 14. The average crystal sizes of the main species are listed in Table 7. All the regenerated catalysts show similar peaks with fresh catalysts (Fig. 5), indicating that the catalysts are successfully regenerated. CaO diffraction peaks appear in all catalysts after the 5th cycle, which is due to the internal CaO being wrapped by gradually formed $CaCO_3$ shells and hindering the further carbonation of CaO [67]. In addition, compared with Ni_1Ca_5 catalyst, the crystal sizes of Ni, CeO_2, and $CaCO_3$ in $Ce_{0.7}Ni_1Ca_5$ catalyst are much smaller and decrease with cycle time, whereas the Ni crystal size in Ni_1Ca_5 increases obviously with cycle time due to agglomeration of

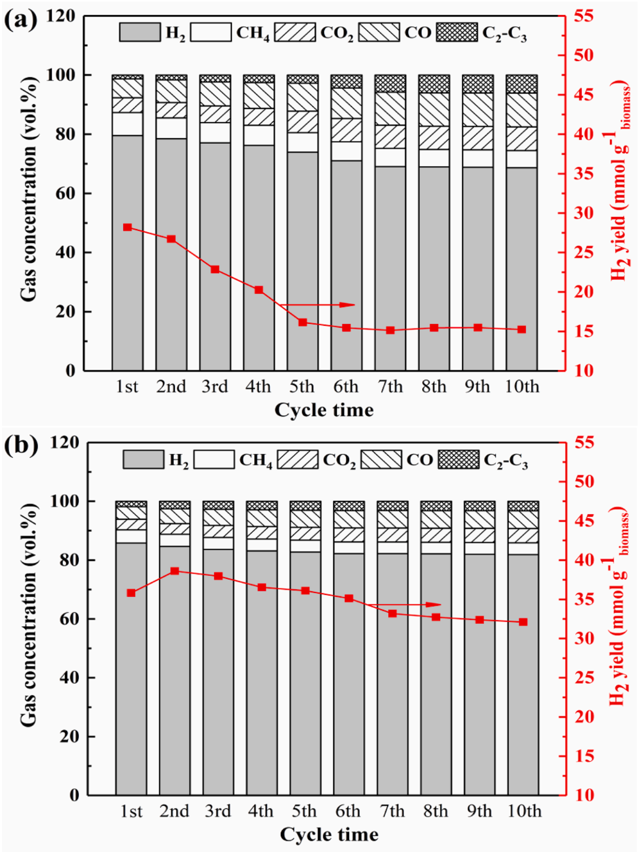

Fig. 13. Gas distribution and H_2 yield in cyclic test with Ni_1Ca_5 (a) and $Ce_{0.7}Ni_1Ca_5$ (b) catalyst.

Table 7
Average crystal size of the first regenerated catalysts and used catalysts after the 5th and 10th time.

Catalyst	Average crystal size (nm)[a]												
	Regenerated			5th time					10th time				
	NiO	CeO_2	CaO	NiO	Ni	CeO_2	CaO	$CaCO_3$	NiO	Ni	CeO_2	CaO	$CaCO_3$
Ni_1Ca_5	22.01	/	28.79	17.60	21.55	/	24.68	21.15	17.60	29.47	/	28.79	18.80
$Ce_{0.7}Ni_1Ca_5$	17.60	18.56	24.68	14.67	12.63	21.11	22.94	18.80	14.67	11.05	18.76	24.68	16.92

[a] Calculated by Scherrer equation based on the diffraction peaks in Fig. 14 at 2θ around 43.2° (NiO), 44.4° (Ni), 28.5° (CeO_2), 37.3° (CaO), and 29.3° ($CaCO_3$), respectively.

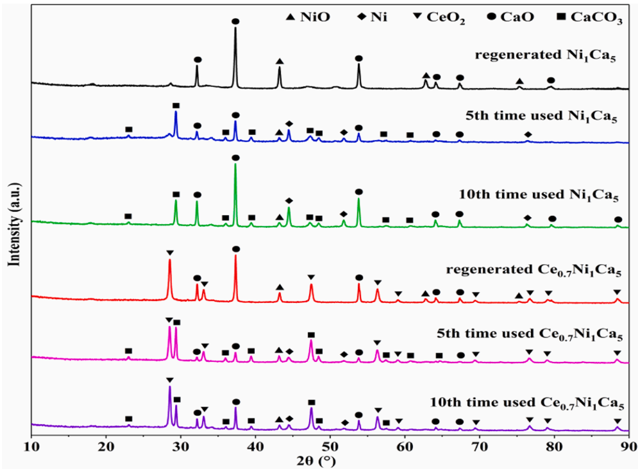

Fig. 14. XRD spectra of the first regenerated catalysts and used catalysts after the 5th and 10th time.

metallic Ni. On the other hand, CaO crystal size increases after the 5th cycle but the size increase of CaO in $Ce_{0.7}Ni_1Ca_5$ is slighter and lower than that in Ni_1Ca_5, as mentioned above, CeO_2 affects the carbonation degree of CaO and hence the decreasing crystal size of $CaCO_3$ and CaO. It can be concluded that $Ce_{0.7}Ni_1Ca_5$ catalyst can effectively prevent the sintering and delay aggregation of CaO species and thus stabilize CaO carbonation and CO_2 sorption after 5 cycles.

SEM images of the used catalysts after the 5th and 10th time are presented in Fig. 15. There is an obvious aggregation of $CaCO_3$ and Ni particles with cycle time in Ni_1Ca_5 catalyst, and the porous structure is almost disappeared after 10 cycles. While $Ce_{0.7}Ni_1Ca_5$ still exhibits a slit-shaped porous structure with slightly metal particles aggravation after 10 cycles.

TEM, HRTEM, and elemental mappings of the used catalysts after 10 cycles as shown in Fig. 16. The exposed planes of Ni (1 1 1) [68] and CeO_2 (1 1 1) with an interplanar spacing of 2.04 Å and 3.12 Å, respectively, were calculated from HRTEM images. TEM images and statistical results of particle distribution (Fig. 16a-f) show that the Ni average particle size of Ni_1Ca_5 is more than twice larger than that of $Ce_{0.7}Ni_1Ca_5$, and element mappings (Fig. 16g-k) also present more obvious agglomeration of Ni particles and consequently decrease of active metal sites on the Ni_1Ca_5 catalyst. While $Ce_{0.7}Ni_1Ca_5$ still exhibits uniform dispersion of metal particles (Fig. 16l-q) after 10 cycles and the Ni particle size is slightly increased.

3.5. *Investigation on carbon deposition of $Ce_{0.7}Ni_1Ca_5$ catalyst*

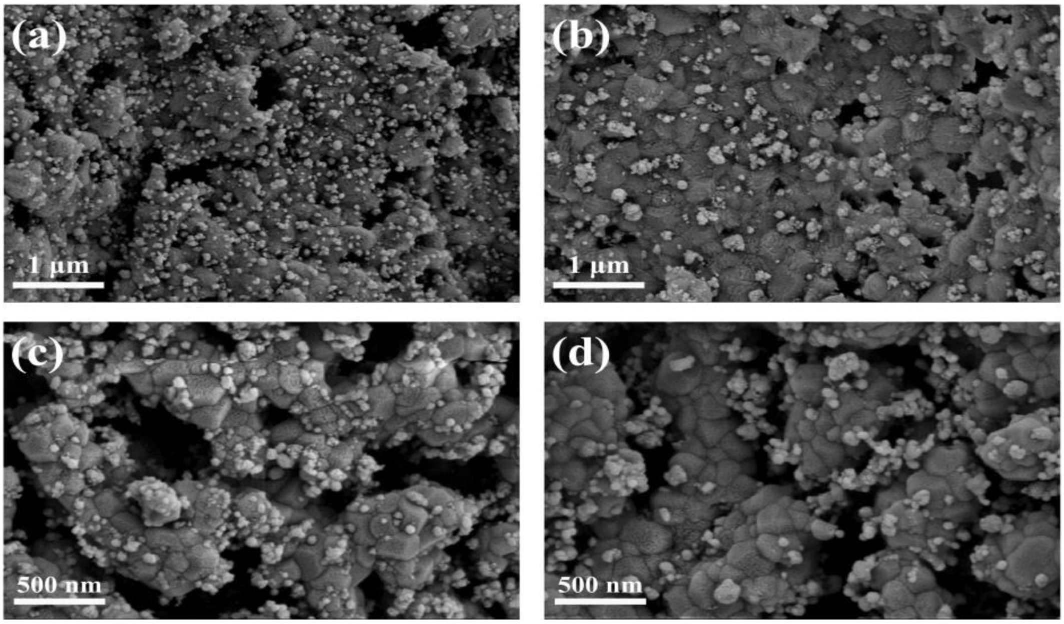

Fig. 15. SEM images of the 5th time used Ni_1Ca_5 (a),10th time used Ni_1Ca_5 (b), 5th time used $Ce_{0.7}Ni_1Ca_5$ (c), and 10th time used $Ce_{0.7}Ni_1Ca_5$ (d).

Fig. 17 shows the TG and DTG thermograms of Ni_1Ca_5 and $Ce_{0.7}Ni_1Ca_5$ catalysts used after the 1st, 5th, and 10th time. In air atmosphere, a slight increase of mass at the first range of 300–450 °C is ascribed to the oxidation of metallic Ni, and the mass gain increases with the cycle time owing to the complete reduction of NiO to metallic Ni after 5 cycles, which can be confirmed by the XRD results (Fig. 14). For $Ce_{0.7}Ni_1Ca_5$ catalyst, the mass gain linked to the oxidation of Ni is less due to the smaller and more stable Ni crystal size compared with Ni_1Ca_5 (Table 7). The mass loss related to the oxidation of deposited amorphous carbon decreases with the cycle time at the second range of 400–550 °C. The

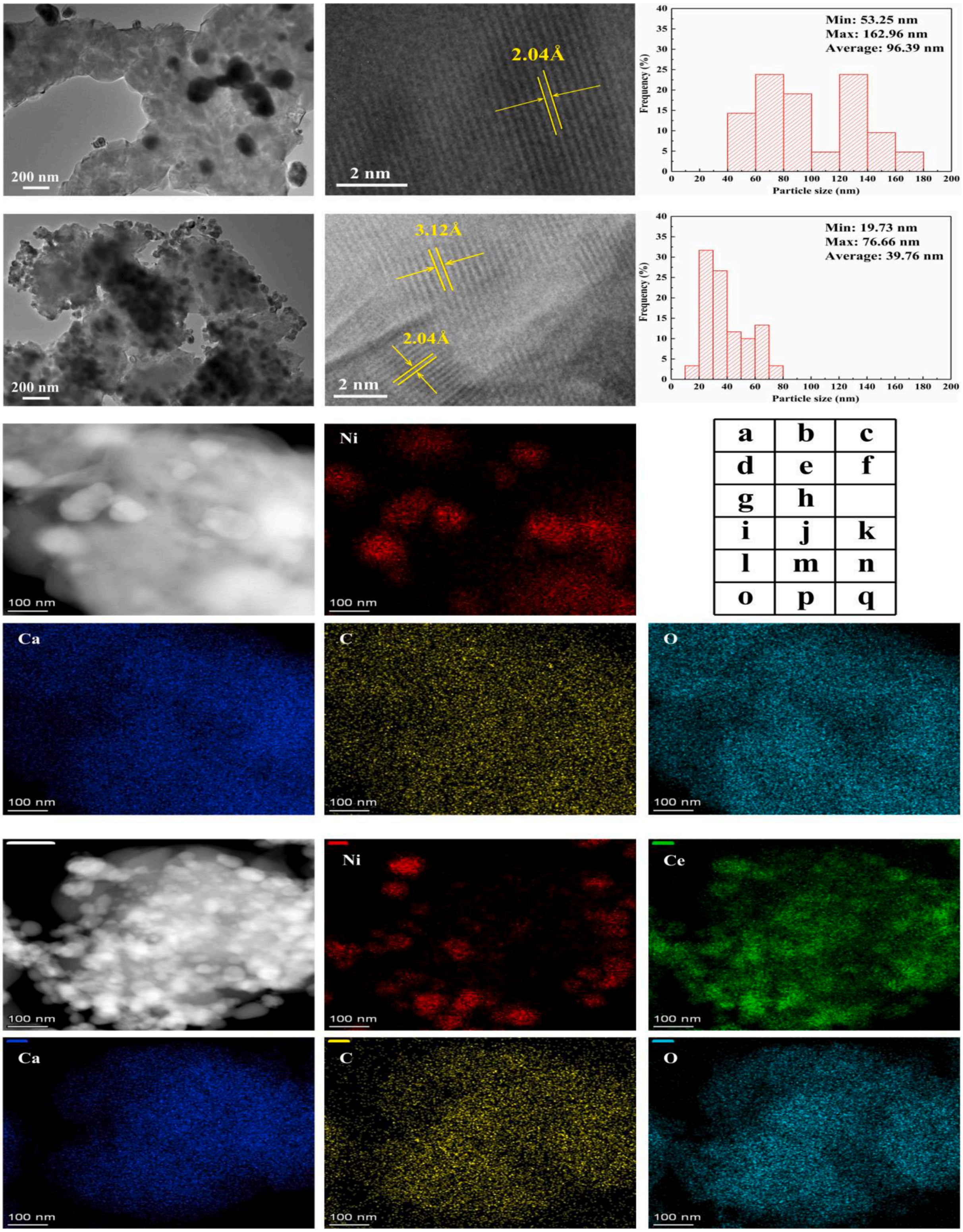

Fig. 16. TEM, HRTEM images, and Ni particle distributions of Ni_1Ca_5 (a)-(c), $Ce_{0.7}Ni_1Ca_5$ (d)-(f), and elemental mappings of Ni_1Ca_5 (g)-(k), $Ce_{0.7}Ni_1Ca_5$ (l)-(q) used after 10 cycles.

remarkable mass loss at the third range of 550–800 °C represents the decomposition of $CaCO_3$ and oxidation of deposited filamentous carbon. For Ni_1Ca_5 catalyst, DTG curves in air show that the weight loss peak at the second and third range both shift toward higher temperatures with the cycle time, but the weight loss peak temperature of $CaCO_3$ decomposition in N_2 becomes lower after 5 cycles, which suggests that, on the one hand, the nature of deposited carbon on the used Ni_1Ca_5 catalyst might be changed to more crystalline carbon (graphite or carbon nanotubes), which would be further determined by Raman analysis in the next section. On the other hand, the larger (sintered) CaO species may only form a $CaCO_3$ shell with the CaO core not being completely carbonized on the regenerated Ni_1Ca_5, resulting in the easier

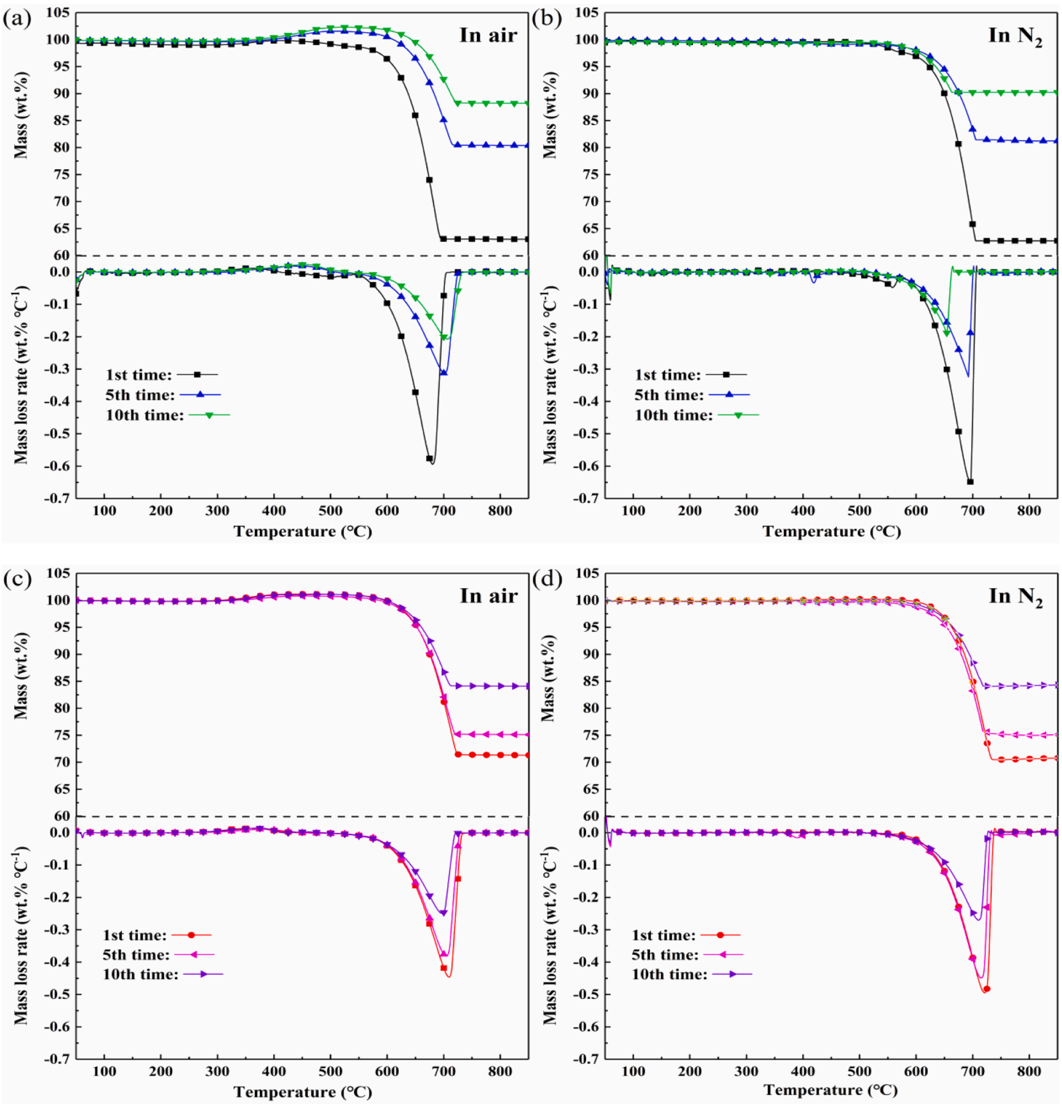

Fig. 17. TG and DTG thermograms in air and N_2 atmosphere of Ni_1Ca_5 (a)-(b) and $Ce_{0.7}Ni_1Ca_5$ (c)-(d) used after the 1st, 5th, and 10th time.

decomposition of $CaCO_3$ and its production decreases with the cycle time. Unlike Ni_1Ca_5 catalyst, $Ce_{0.7}Ni_1Ca_5$ generates more stable $CaCO_3$, and the nature of its deposited carbon is unchanged with the cycle time.

The amount of $CaCO_3$ and deposited carbon were calculated and listed in Table 8. The results show that the carbon deposition of $Ce_{0.7}Ni_1Ca_5$ is only about 30% of that of Ni_1Ca_5 after 10 cycles and hardly increased after 5 cycles. In addition, the $CaCO_3$ production of $Ce_{0.7}Ni_1Ca_5$ used after 5 cycles becomes higher than that of Ni_1Ca_5 and even exceed nearly 80% after 10 cycles, suggesting that the $CaCO_3$ production of $Ce_{0.7}Ni_1Ca_5$ decreases more slowly with the cycle time, which further demonstrates that the CO_2 sorption capacity of $Ce_{0.7}Ni_1Ca_5$ is more stable and much higher than that of Ni_1Ca_5 after 5 cycles, which also agrees with the result of stable and lower CO_2 yield of $Ce_{0.7}Ni_1Ca_5$ in Fig. 13.

Table 8
Amount of deposited carbon and $CaCO_3$ of the used catalysts after the 1st, 5th, and 10th time.

	Ni_1Ca_5			$Ce_{0.7}Ni_1Ca_5$		
	1st time	5th time	10th time	1st time	5th time	10th time
Deposited carbon (mg $g^{-1}_{catalyst}$)	21.13	37.51	55.68	6.01	15.10	16.76
$CaCO_3$ (mg $g^{-1}_{catalyst}$)	349.59	174.35	85.45	292.72	241.88	153.53

The molecular structure of deposited carbon on the used catalysts after 10 cycles were identified by combining XPS spectra for C1s (Fig. 18) and FTIR spectra (Fig. 19). Raman spectra (Fig. 20) were used to further analyze the carbon species and degree of graphitization. Considering the high sensitivity in surface analysis of XPS and FTIR for the possible adsorbed H_2O, CO_2, and adventitious carbon from the air on the catalysts during storage, transportation, and characterization, the comparison between fresh catalysts following air exposure and used catalysts is necessary to elaborate the chemical properties of carbon deposited on the surface of used catalysts.

Fig. 18(b) shows that both the used Ni_1Ca_5 and $Ce_{0.7}Ni_1Ca_5$ catalysts present three peaks corresponding to C—C (aromatic group, 284.6 eV), C—O—C (ketone group, 287.5 eV), and O—C═O (ester group or carbonates, 289.5 eV) components [69], respectively, which are stronger than those of fresh catalysts (Fig. 18a), suggesting that more carbonates, ketone compounds, and aromatic carbon deposited on the used catalyst surface. Although there is no obvious difference in C1s peak between all fresh catalysts, for the used catalysts (Fig. 18b), the most intense C—C peak in Ni_1Ca_5 is higher than that of $Ce_{0.7}Ni_1Ca_5$, indicating that the carbon deposited on the used catalysts mainly contains aromatic

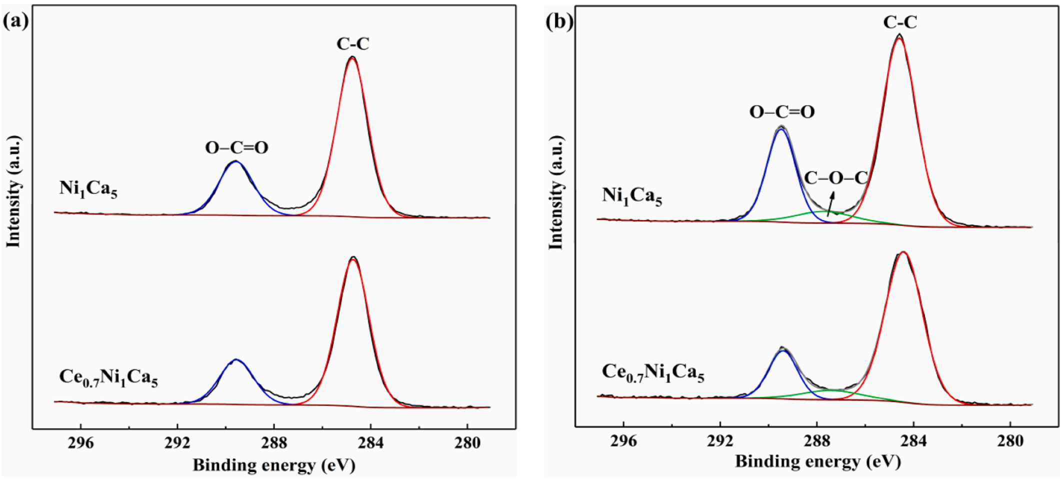

Fig. 18. XPS spectra for C1s of the fresh catalysts following air exposure (a) and used catalysts after 10 cycles (b).

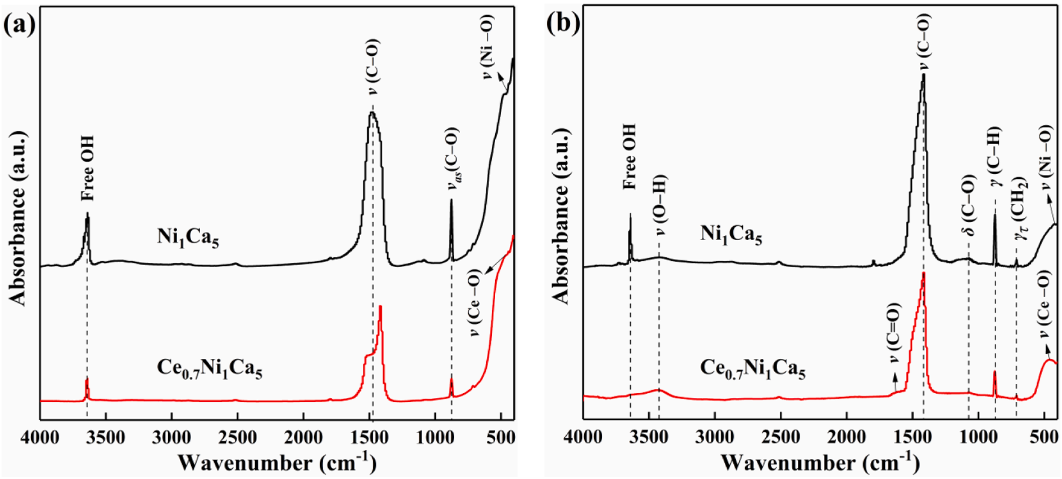

Fig. 19. FTIR spectra of the fresh catalysts following air exposure (a) and used catalysts after 10 cycles (b).

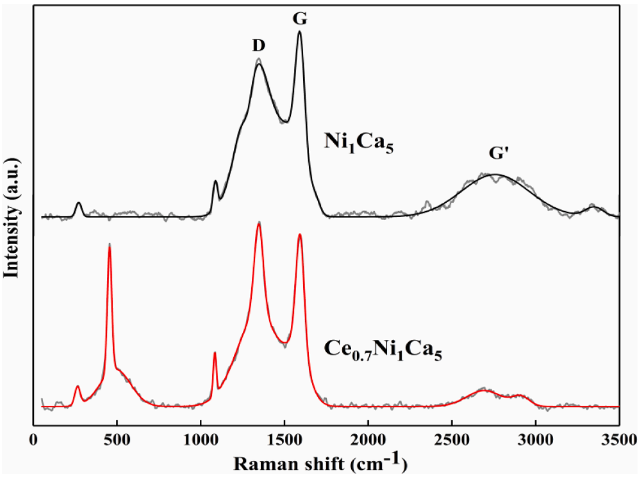

Fig. 20. Raman spectra of the used catalysts after 10 cycles.

compounds and its content in Ni_1Ca_5 is slightly higher than that in $Ce_{0.7}Ni_1Ca_5$.

Fig. 19 shows FTIR spectra of the catalysts, the assignment of absorption bands are based on the information in references [70–75]. For the fresh catalysts following air exposure (Fig. 19a), the absorption peaks located at 465 and 873 cm^{-1} are characteristics of CeO_2 and can be ascribed to ν(Ce-O) stretching vibrations [71] for $Ce_{0.7}Ni_1Ca_5$, and Ni_1Ca_5 possesses a characteristic peak at 470 cm^{-1} assigned to ν(Ni-O) stretch [72]. The peaks at 875 and 1420 cm^{-1} corresponding to ν(C-O) stretch are related to carbonates or hydrocarbonates [73], and the peaks at 3640 cm^{-1} corresponding to free OH of water [74] are observed in both catalysts. Compared with the fresh catalysts, the used catalysts show a stronger absorption peak of ν(C-O) and weaker peaks assigned to CeO_2 and NiO as shown in Fig. 19b, suggesting that more CO_2 was adsorbed by the used catalysts accompanied by the decrease of CeO_2 and NiO species owing to reduction. For the used catalysts (Fig. 19b), compared with those of Ni_1Ca_5, $Ce_{0.7}Ni_1Ca_5$ contains weaker peaks at 712, 875, 1080, and 1415 cm^{-1} corresponding to $\gamma_\tau(CH_2)$ rocking vibration, γ(C—H) bending of aromatic compounds, δ(C—O) deformation of secondary alcohols and aliphatic ethers, and ν(C—O) stretching mode, respectively. The peak at 3640 cm^{-1} associated with free OH in Ni_1Ca_5 is not observed in $Ce_{0.7}Ni_1Ca_5$. Apart from that, $Ce_{0.7}Ni_1Ca_5$ shows slightly stronger peaks at 3420 cm^{-1} corresponding to ν(O—H) stretch and 1605–1593 cm^{-1} corresponding to ν(C=O) stretch than Ni_1Ca_5, which can be attributed to alcohols, phenols, acids, ketones, and bidentate carbonates [70,75]. These results also indicate that Ni_1Ca_5 contains more aromatic or aliphatic compounds than $Ce_{0.7}Ni_1Ca_5$ used after 10 cycles.

Fig. 20 shows Raman spectra of the used catalysts. The peak at around 465 cm^{-1} in $Ce_{0.7}Ni_1Ca_5$ usually belongs to CeO_2 single crystal

[76]. There is a small peak at around 1088 cm^{-1} assigned to ν_{as}(C—O) asymmetric stretch both in Ni_1Ca_5 and $Ce_{0.7}Ni_1Ca_5$, which belongs to the CO_3^{2-} of $CaCO_3$ [77]. The D band at 1200–1400 cm^{-1} and G band at 1400–1700 cm^{-1} are ascribed to the vibration of amorphous carbon and graphite sheet, respectively [78]. The intensity of the G' band at 2500–2700 cm^{-1} is related to the two-photon elastic scattering and is usually used to measure the purity of deposited carbon [79]. The G peak is stronger than the D peak in Ni_1Ca_5. On the contrary, the $Ce_{0.7}Ni_1Ca_5$ catalyst displays a larger D peak than G peak, indicating that more amorphous carbon than graphite is produced by the used $Ce_{0.7}Ni_1Ca_5$. Moreover, the smaller G' band suggests that the used $Ce_{0.7}Ni_1Ca_5$ generates less graphitic carbon species with lower purity and degree of graphitization. This founding agrees well with the result of DTG in Fig. 17, which shows the oxidation temperature of deposited amorphous and filamentous/graphite carbon on $Ce_{0.7}Ni_1Ca_5$ after 10 cycles are about 420 °C and 690 °C, respectively, which is relatively lower than that of Ni_1Ca_5 after 10 cycles (amorphous carbon oxidized at 525 °C and filamentous/graphite carbon oxidized at 708 °C). It can be concluded that the oxidation temperature of deposited carbon (especially amorphous carbon) is significantly reduced by the doping of Ce, which is attributed to the high oxygen transport capacity of CeO_2 promoting the reforming of deposited carbon by providing it necessary active oxygen species [39].

4. Conclusion

$Ce_{0.7}Ni_1Ca_5$ catalyst exhibits the best performance among all prepared catalysts by achieving the highest H_2 concentration (85.81 (±0.39) vol.%) and H_2 yield (35.82(±0.28) mmol $g^{-1}_{biomass}$) under a condition of 500 °C, S/C = 5 (mol/mol), and catalyst/biomass = 2.5 (g/g), producing the lowest content of CO_2 (3.62(±0.16) vol.%), CO (4.27 (±0.11) vol.%), CH_4 (4.49(±0.18) vol.%), and C_2-C_3 (1.81(±0.09) vol.%), correspondingly, which is attributed to the favorable pore expansion ability and sintering inhibition of CeO_2, leading to the small particle size of NiO dispersed uniformly on the CaO matrix with the largest pore volume and specific surface area. Meanwhile, the strong Ni-O-Ce interaction induces the creation of oxygen vacancies that facilitate the fracture of O–H bonds of water for the formation of H_2. In addition, WGS and SMR reactions are both promoted by CeO_2 to produce more hydrogen, resulting in lower contents of CO and CH_4 but slightly higher contents of C_2–C_3. The catalyst/biomass mass ratio of 2.5 is deemed optimal considering there are enough residence time for steam reforming of derived gases into H_2 and lower catalytic cost. In addition, $Ce_{0.7}Ni_1Ca_5$ exhibits stable catalytic activity in H_2 production, CO_2 sorption, and inhibition of carbon deposition. The H_2 concentration and H_2 yield remain above 81.88 vol% and 32.11 mmol $g^{-1}_{biomass}$ respectively during 10 cyclic tests, which is almost twice that achieved by Ni_1Ca_5 catalyst. Well-dispersed CeO_2 can effectively prevent the sintering and delay aggregation of CaO species, resulting in stable CaO carbonation and the CO_2 emission keeps below 4.85 vol% during 10 cycles. The amount of deposited carbon on the surface of $Ce_{0.7}Ni_1Ca_5$ used for 10 cycles is only about 30% of that of Ni_1Ca_5 and hardly increased after 5 cycles, which is attributed to that the high oxygen transport capacity of CeO_2 is responsible for reforming the deposited carbon by lowering the oxidation temperature of amorphous carbon containing low-molecular aromatic or aliphatic compounds with lower degree of graphitization.

Declaration of Competing Interest

The authors declare that they have no known competing financial interests or personal relationships that could have appeared to influence the work reported in this paper.

Acknowledgement

This work was supported by the National Key R&D Program of China (No: 2018YFB0605000).

References

[1] D. Das, T. Veziroglu, Advances in biological hydrogen production processes, Int. J. Hydrogen Energy 33 (21) (2008) 6046–6057, https://doi.org/10.1016/j.ijhydene.2008.07.098.

[2] P. Parthasarathy, K.S. Narayanan, Hydrogen production from steam gasification of biomass: influence of process parameters on hydrogen yield-A review, Renew. Energ. 66 (2014) 570–579, https://doi.org/10.1016/j.renene.2013.12.025.

[3] A. Arregi, M. Amutio, G. Lopez, J. Bilbao, M. Olazar, Evaluation of thermochemical routes for hydrogen production from biomass: A review, Energ. Convers. Manage. 165 (2018) 696–719, https://doi.org/10.1016/j.enconman.2018.03.089.

[4] B. Pandey, Y.K. Prajapati, P.N. Sheth, Recent progress in thermochemical techniques to produce hydrogen gas from biomass: a state of the art review, Int. J. Hydrogen Energ. 44 (47) (2019) 25384–25415, https://doi.org/10.1016/j.ijhydene.2019.08.031.

[5] U. Çolak, H. Durak, S. Genel, Hydrothermal liquefaction of Syrian mesquite (Prosopis farcta): effects of operating parameters on product yields and characterization by different analysis methods, J. Supercrit. Fluids 140 (2018) 53–61, https://doi.org/10.1016/j.supflu.2018.05.027.

[6] H. Durak, Characterization of products obtained from hydrothermal liquefaction of biomass (Anchusa azurea) compared to other thermochemical conversion methods, Biomass Convers. Biorefinery 9 (2) (2019) 459–470, https://doi.org/10.1007/s13399-019-00379-4.

[7] H. Durak, S. Genel, Catalytic hydrothermal liquefaction of lactuca scariola with a heterogeneous catalyst: the investigation of temperature, reaction time and synergistic effect of catalysts, Bioresour. Technol. 309 (2020) 123375, https://doi.org/10.1016/j.biortech.2020.123375.

[8] Y.A. Situmorang, Z. Zhao, A. Yoshida, A. Abudula, G. Guan, Small-scale biomass gasification systems for power generation (<200 kW class): A review, Renew. Sustain. Energy Rev. 117 (2020), 109486, https://doi.org/10.1016/j.rser.2019.109486.

[9] D.O. Albina, Emissions from multiple-spouted and spout-fluid fluidized beds using rice husks as fuel, Renew Energ. 31 (13) (2006) 2152–2163, https://doi.org/10.1016/j.renene.2006.02.013.

[10] R.S. Prakasham, T. Sathish, P. Brahmaiah, C.h. Subba Rao, R. Sreenivas Rao, P. J. Hobbs, Biohydrogen production from renewable agri-waste blend: optimization using mixer design, Int. J. Hydrogen Energ. 34 (15) (2009) 6143–6148, https://doi.org/10.1016/j.ijhydene.2009.06.016.

[11] M. Prestipino, A. Galvagno, O. Karlström, A. Brink, Energy conversion of agricultural biomass char: steam gasification kinetics, Energy 161 (2018) 1055–1063, https://doi.org/10.1016/j.energy.2018.07.205.

[12] Y. Sun, J. Chen, Z. Zhang, Biomass gasification using the waste heat from high temperature slags in a mixture of CO_2 and H_2O, Energy 167 (2019) 688–697, https://doi.org/10.1016/j.energy.2018.11.019.

[13] J.G. Olsson, J.B.C. Pettersson, N. Padban, I. Bjerle, Alkali metal emission from filter ash and fluidized bed material from PFB gasification of biomass, Energy Fuels 12 (3) (1998) 626–630, https://doi.org/10.1021/ef970211y.

[14] N.H. Florin, A.T. Harris, Enhanced hydrogen production from biomass with in situ carbon dioxide capture using calcium oxide sorbents, Chem. Eng. Sci. 63 (2) (2008) 287–316, https://doi.org/10.1016/j.ces.2007.09.011.

[15] M. Shokrollahi Yancheshmeh, H.R. Radfarnia, M.C. Iliuta, High temperature CO_2 sorbents and their application for hydrogen production by sorption enhanced steam reforming process, Chem. Eng. J. 283 (2016) 420–444, https://doi.org/10.1016/j.cej.2015.06.060.

[16] V. Materic, S.I. Smedley, High temperature carbonation of $Ca(OH)_2$, Ind. Eng. Chem. Res. 50 (10) (2011) 5927–5932, https://doi.org/10.1021/ie200367w.

[17] C.J. Knill, J.F. Kennedy, Degradation of cellulose under alkaline conditions, Carbohyd. Polym. 51 (3) (2003) 281–300, https://doi.org/10.1016/S0144-8617(02)00183-2.

[18] M. Zheng, J. Pang, R. Sun, A. Wang, T. Zhang, Selectivity control for cellulose to diols: dancing on eggs, ACS Catal. 7 (3) (2017) 1939–1954, https://doi.org/10.1021/acscatal.6b03469.

[19] C. Wu, P.T. Williams, A novel Ni-Mg-Al-CaO catalyst with the dual functions of catalysis and CO_2 sorption for H_2 production from the pyrolysis–gasification of polypropylene, Fuel 89 (7) (2010) 1435–1441, https://doi.org/10.1016/j.fuel.2009.10.020.

[20] X. Zhao, Y. Xue, C. Yan, Z. Wang, C. Guo, S. Huang, Sorbent assisted catalyst of Ni-CaO-La_2O_3 for sorption enhanced steam reforming of bio-oil with acetic acid as the model compound, Chem. Eng. Process.: Process Intensification 119 (2017) 106–112, https://doi.org/10.1016/j.cep.2017.05.012.

[21] G. Chen, J. Yao, J. Liu, B. Yan, R. Shan, Biomass to hydrogen-rich syngas via catalytic steam gasification of bio-oil/biochar slurry, Bioresour. Technol. 198 (2015) 108–114, https://doi.org/10.1016/j.biortech.2015.09.009.

[22] J. Zou, H. Yang, Z. Zeng, C. Wu, P.T. Williams, H. Chen, Hydrogen production from pyrolysis catalytic reforming of cellulose in the presence of K alkali metal, Int. J. Hydrogen Energ. 41 (25) (2016) 10598–10607, https://doi.org/10.1016/j.ijhydene.2016.04.207.

[23] Y. Tursun, S. Xu, A. Abulikemu, T. Dilinuer, Biomass gasification for hydrogen rich gas in a decoupled triple bed gasifier with olivine and NiO/olivine, Bioresour. Technol. 272 (2019) 241–248, https://doi.org/10.1016/j.biortech.2018.10.008.

[24] T.N.L.T. Ngo, K.-Y. Chiang, C.-F. Liu, Y.-H. Chang, H.-P. Wan, Hydrogen production enhancement using hot gas cleaning system combined with prepared Ni-based catalyst in biomass gasification, Int. J. Hydrogen Energ. 46 (20) (2021) 11269–11283, https://doi.org/10.1016/j.ijhydene.2020.08.279.

[25] X. Zeng, M. Fang, T. Lv, J. Tian, Z. Xia, J. Cen, Q. Wang, Enhanced hydrogen production by the catalytic alkaline thermal gasification of cellulose with Ni/Fe dual-functional CaO based catalysts, Int. J. Hydrogen Energ. 46 (65) (2021) 32783–32799, https://doi.org/10.1016/j.ijhydene.2021.07.142.

[26] A.S.A. Al-fatesh, A.H. Fakeeha, A.E. Abasaeed, Effects of Selected Promoters on Ni/Y-Al_2O_3 catalyst performance in methane dry reforming, Chinese J. Catal. 32 (9-10) (2011) 1604–1609, https://doi.org/10.1016/S1872-2067(10)60267-7.

[27] Q. Li, S. Ji, J. Hu, S. Jiang, Catalytic steam reforming of rice straw biomass to hydrogen-rich syngas over Ni-based catalysts, Chinese J. Catal. 34 (7) (2013) 1462–1468, https://doi.org/10.1016/S1872-2067(12)60618-4.

[28] A.A. Rownaghi, R.L. Huhnke, Producing hydrogen-rich gases by steam reforming of syngas tar over CaO/MgO/NiO catalysts, ACS Sustain. Chem. Eng. 1 (1) (2013) 80–86, https://doi.org/10.1021/sc300042e.

[29] R.S. Tan, T.A. Tuan Abdullah, S.A. Mahmud, R. Md Zin, K. Md Isa, Catalytic steam reforming of complex gasified biomass tar model toward hydrogen over dolomite promoted nickel catalysts, Int. J. Hydrogen Energ. 44 (39) (2019) 21303–21314, https://doi.org/10.1016/j.ijhydene.2019.06.125.

[30] S. Scaccia, L. Della Seta, D. Mirabile Gattia, G. Vanga, Catalytic performance of Ni/CaO-$Ca_{12}Al_{14}O_{33}$ catalyst in the green synthesis gas production via CO_2 reforming of CH_4, J. CO_2 Util. 45 (2021) 101447, https://doi.org/10.1016/j.jcou.2021.101447.

[31] M.S. Duyar, S. Wang, M.A. Arellano-Treviño, R.J. Farrauto, CO_2 utilization with a novel dual function material (DFM) for capture and catalytic conversion to synthetic natural gas: An update, J. CO_2 Util. 15 (2016) 65–71, https://doi.org/10.1016/j.jcou.2016.05.003.

[32] J.P.d.S.Q. Menezes, F.C. Jácome, R.L. Manfro, M.M.V.M. Souza, Effect of CaO addition on nickel catalysts supported on alumina for glycerol steam reforming, Catal. Lett. 149 (7) (2019) 1991–2003, https://doi.org/10.1007/s10562-019-02792-w.

[33] S.F. Wu, L.L. Wang, Improvement of the stability of a ZrO_2-modified Ni-nano-CaO sorption complex catalyst for ReSER hydrogen production, Int. J. Hydrogen Energ. 35 (13) (2010) 6518–6524, https://doi.org/10.1016/j.ijhydene.2010.03.120.

[34] M.R. Stonor, N. Ouassil, J.G. Chen, A.-H. Park, Investigation of the role of $Ca(OH)_2$ in the catalytic Alkaline Thermal Treatment of cellulose to produce H_2 with integrated carbon capture, J. Energy Chem. 26 (5) (2017) 984–1000, https://doi.org/10.1016/j.jechem.2017.07.013.

[35] M.R. Stonor, T.E. Ferguson, J.G. Chen, A. Park, Biomass conversion to H_2 with substantially suppressed CO_2 formation in the presence of Group I & Group II hydroxides and a Ni/ZrO_2 Catalyst, Energ Environ. Sci. 8 (2015) 1702–1706, https://doi.org/10.1039/C4EE04103H.

[36] M.F.A. Khan, A. Khan, H. Ibrahim, R. Idem, Kinetic study of the catalytic partial oxidation of synthetic diesel over 5 wt % Ni/$Ce_{0.5}Zr_{0.33}Ca_{0.085}Y_{0.085}O_{2\text{-}\delta}$ catalyst for hydrogen production, Energy Fuel. 26 (9) (2012) 5421–5429, https://doi.org/10.1021/ef301075y.

[37] C. Wu, Z. Wang, J. Huang, P.T. Williams, Pyrolysis/gasification of cellulose, hemicellulose and lignin for hydrogen production in the presence of various nickel-based catalysts, Fuel 106 (2013) 697–706, https://doi.org/10.1016/j.fuel.2012.10.064.

[38] Q.M.K. Waheed, P.T. Williams, Hydrogen production from high temperature pyrolysis/steam reforming of waste biomass: rice husk, sugar cane bagasse, and wheat straw, Energ Fuel. 27 (11) (2013) 6695–6704, https://doi.org/10.1021/ef401145w.

[39] J. Ashok, S. Kawi, Steam reforming of toluene as a biomass tar model compound over CeO_2 promoted Ni/CaO-Al_2O_3 catalytic systems, Int. J. Hydrogen Energ. 38 (32) (2013) 13938–13949, https://doi.org/10.1016/j.ijhydene.2013.08.029.

[40] J. Phromprasit, J. Powell, S. Wongsakulphasatch, W. Kiatkittipong, P. Bumroongsakulsawat, S. Assabumrungrat, H_2 production from sorption enhanced steam reforming of biogas using multifunctional catalysts of Ni over Zr-, Ce- and La-modified CaO sorbents, Chem. Eng. J. 313 (2017) 1415–1425, https://doi.org/10.1016/j.cej.2016.11.051.

[41] M. Shokrollahi Yancheshmeh, H.R. Radfarnia, M.C. Iliuta, Sustainable production of high-purity hydrogen by sorption enhanced steam reforming of glycerol over CeO_2-promoted $Ca_9Al_6O_{18}$-CaO/NiO Bifunctional Material, ACS Sustain. Chem. Eng. 5 (11) (2017) 9774–9786, https://doi.org/10.1021/acssuschemeng.7b01627.

[42] R.R. Davda, J.W. Shabaker, G.W. Huber, R.D. Cortright, J.A. Dumesic, A review of catalytic issues and process conditions for renewable hydrogen and alkanes by aqueous-phase reforming of oxygenated hydrocarbons over supported metal catalysts, Appl. Catal. B: Environ. 56 (1-2) (2005) 171–186, https://doi.org/10.1016/j.apcatb.2004.04.027.

[43] M. Ni, D.Y.C. Leung, M.K.H. Leung, A review on reforming bio-ethanol for hydrogen production, Int. J. Hydrogen Energ. 32 (15) (2007) 3238–3247, https://doi.org/10.1016/j.ijhydene.2007.04.038.

[44] S. Wang, S. Fan, L. Fan, Y. Zhao, X. Ma, Effect of cerium oxide doping on the performance of CaO-based sorbents during calcium looping cycles, Environ. Sci. Technol. 49 (8) (2015) 5021–5027, https://doi.org/10.1021/es5052843.

[45] J. Zou, J. Oladipo, S. Fu, A. Al-Rahbi, H. Yang, C. Wu, N. Cai, P. Williams, H. Chen, Hydrogen production from cellulose catalytic gasification on CeO_2/Fe_2O_3 catalyst, Energ. Convers Manage. 171 (2018) 241–248, https://doi.org/10.1016/j.enconman.2018.05.104.

[46] K.S.W. Sing, Reporting physisorption data for gas/solid systems with special reference to the determination of surface area and porosity (Recommendations 1984), Pure Appl. Chem. 57 (4) (1985) 603–619, https://doi.org/10.1351/pac198557040603.

[47] H. Sun, J. Wang, J. Zhao, B. Shen, J. Shi, J. Huang, and C. Wu, Dual functional catalytic materials of Ni over Ce-modified CaO sorbents for integrated CO_2 capture and conversion, Applied Catalysis B: Environmental 244 (2019) 63-75, doi: 10.1016/j.apcatb.2018.11.040.

[48] M. Zhang, Y. Peng, Y. Sun, P. Li, J. Yu, Preparation of CaO-Al_2O_3 sorbent and CO_2 capture performance at high temperature, Fuel 111 (2013) 636–642, https://doi.org/10.1016/j.fuel.2013.03.078.

[49] H. Roh, I. Eum, D. Jeong, Low temperature steam reforming of methane over Ni-$Ce_{(1-x)}Zr_{(x)}O_2$ catalysts under severe conditions, Renew. Energ. 42 (2012) 212–216, https://doi.org/10.1016/j.renene.2011.08.013.

[50] A. Dutta, J. Datta, Energy efficient role of Ni/NiO in PdNi nano catalyst used in alkaline DEFC, J. Mater. Chem. A 2 (9) (2014) 3237, https://doi.org/10.1039/c3ta12708g.

[51] S.Y. Shen, T.S. Zhao, J.B. Xu, Y.S. Li, Synthesis of PdNi catalysts for the oxidation of ethanol in alkaline direct ethanol fuel cells, J. Power Sources 195 (4) (2010) 1001–1006, https://doi.org/10.1016/j.jpowsour.2009.08.079.

[52] H. Guo, J. Feng, Y. Zhao, S. Wang, X. Ma, Effect of micro-structure and oxygen vacancy on the stability of (Zr-Ce)-additive CaO-based sorbent in CO_2 adsorption, J. CO_2 Util. 19 (2017) 165–176, https://doi.org/10.1016/j.jcou.2017.03.015.

[53] Z. Fang, B. Yuan, T. Lin, H. Xu, Y. Cao, Z. Shi, M. Gong, Y. Chen, Monolith $Ce_{0.65}Zr_{0.35}O_2$-based catalysts for selective catalytic reduction of NO_x with NH_3, Chem. Eng. Res. Des. 94 (2015) 648–659, https://doi.org/10.1016/j.cherd.2014.10.006.

[54] F. Larachi, J. Pierre, A. Adnot, A. Bernis, Ce 3d XPS study of composite $Ce_xMn_{1\text{-}x}O_{2\text{-}y}$ wet oxidation catalysts, Appl. Surf. Sci. 195 (1-4) (2002) 236–250, https://doi.org/10.1016/S0169-4332(02)00559-7.

[55] M. Lopezgranados, A. Gurbani, R. Mariscal, J. Fierro, Deterioration of the oxygen storage and release properties of $CeZrO_4$ by incorporation of calcium, J. Catal. 256 (2) (2008) 172–182, https://doi.org/10.1016/j.jcat.2008.03.011.

[56] D. Li, Y. Gong, Y. Zhang, C. Luo, W. Li, Q. Fu, C. Pan, Facile synthesis of carbon nanosphere/$NiCo_2O_4$ core-shell sub-microspheres for high performance supercapacitor, Sci. Rep.-UK 5 (2015) 1–8, https://doi.org/10.1038/srep12903.

[57] A. Khan, P. Chen, P. Boolchand, P. Smirniotis, Modified nano-crystalline ferrites for high-temperature WGS membrane reactor applications, J. Catal. 253 (1) (2008) 91–104, https://doi.org/10.1016/j.jcat.2007.10.018.

[58] L. Barrio, A. Kubacka, G. Zhou, M. Estrella, A. Martínez-Arias, J.C. Hanson, M. Fernández-García, J.A. Rodriguez, Unusual physical and chemical properties of Ni in $Ce_{1-x}Ni_xO_{2-y}$Oxides: structural characterization and catalytic activity for the water gas shift reaction, J. Phys. Chem. 114 (29) (2010) 12689–12697, https://doi.org/10.1021/jp103958u.

[59] T. Sukonket, A. Khan, B. Saha, H. Ibrahim, S. Tantayanon, P. Kumar, R. Idem, Influence of the catalyst preparation method, surfactant amount, and steam on CO_2 reforming of CH_4 over 5Ni/$Ce_{0.6}Zr_{0.4}O_2$ catalysts, Energ. Fuel. 25 (3) (2011) 864–877, https://doi.org/10.1021/ef101479y.

[60] G. Zhou, L. Barrio, S. Agnoli, S.D. Senanayake, J. Evans, A. Kubacka, M. Estrella, J. C. Hanson, A. Martínez-Arias, M. Fernández-García, J.A. Rodriguez, High Activity of $Ce_{1-x}Ni_xO_{2-y}$ for H_2 production through ethanol steam reforming: tuning catalytic performance through metal-oxide interactions, Angew. Chem. Int. Ed. 49 (50) (2010) 9680–9684, https://doi.org/10.1002/anie.201004966.

[61] S. Hilaire, X. Wang, T. Luo, R.J. Gorte, J. Wagner, A comparative study of water-gas-shift reaction over ceria supported metallic catalysts, Appl. Catal. A: General 215 (1-2) (2001) 271–278, https://doi.org/10.1016/S0926-860X(01)00535-X.

[62] F. Sadi, D. Duprez, F. Gérard, A. Miloudi, Hydrogen formation in the reaction of steam with Rh/CeO_2 catalysts: a tool for characterising reduced centres of ceria, J. Catal. 213 (2003) 226–234, https://doi.org/10.1016/S0021-9517(02)00080-5.

[63] R.J. Gorte, S. Zhao, Studies of the water-gas-shift reaction with ceria-supported precious metals, Catal. Today 104 (1) (2005) 18–24, https://doi.org/10.1016/j.cattod.2005.03.034.

[64] J. Li, J. Liu, S. Liao, R. Yan, Hydrogen-rich gas production by air-steam gasification of rice husk using supported nano-NiO/γ-Al_2O_3 catalyst, Int. J. Hydrogen Energ. 35 (14) (2010) 7399–7404, https://doi.org/10.1016/j.ijhydene.2010.04.108.

[65] D. Ayillath Kutteri, I.-W. Wang, A. Samanta, L. Li, J. Hu, Methane decomposition to tip and base grown carbon nanotubes and CO_x-free H_2 over mono- and bimetallic 3d transition metal catalysts, Catal. Sci. Technol. 8 (3) (2018) 858–869, https://doi.org/10.1039/C7CY01927K.

[66] J. Xu, C.M.Y. Yeung, J. Ni, F. Meunier, N. Acerbi, M. Fowles, S.C. Tsang, Methane steam reforming for hydrogen production using low water-ratios without carbon formation over ceria coated Ni catalysts, Appl. Catal. A: General 345 (2) (2008) 119–127, https://doi.org/10.1016/j.apcata.2008.02.044.

[67] M. Zhao, J. Shi, X. Zhong, S. Tian, J. Blamey, J. Jiang, P.S. Fennell, A novel calcium looping absorbent incorporated with polymorphic spacers for hydrogen production and CO_2 capture, Energy Environ. Sci. 7 (10) (2014) 3291–3295, https://doi.org/10.1039/C4EE01281J.

[68] D. Yao, H. Yang, H. Chen, P.T. Williams, Co-precipitation, impregnation and so-gel preparation of Ni catalysts for pyrolysis-catalytic steam reforming of waste plastics, Appl. Catal. B: Environmental 239 (2018) 565–577, https://doi.org/10.1016/j.apcatb.2018.07.075.

[69] A.V. Shchukarev, D.V. Korolkov, XPS Study of group IA carbonates, Central Eur. J. Chem. 2 (2004) 347–362, https://doi.org/10.2478/BF02475578.

[70] C. Binet, M. Daturi, J.-C. Lavalley, IR study of polycrystalline ceria properties in oxidised and reduced states, Catal. Today 50 (2) (1999) 207–225, https://doi.org/10.1016/S0920-5861(98)00504-5.

[71] J. Gulicovski, S. Nenadović, L. Kljajević, M. Mirković, M. Nišavić, M. Kragović, M. Stojmenović, Geopolymer/CeO_2 as Solid Electrolyte for IT-SOFC, Polymers-Basel 12 (2020) 248, https://doi.org/10.3390/polym12010248.

[72] A. Rahdar, M. Aliahmad, and A. Y., NiO Nanoparticles: Synthesis and Characterization, Journal of nanostructures 5 (2015), doi:10.7508/jns.2015.02.009.

[73] M.A. Trezza, A.E. Lavat, Analysis of the system $3CaO{\cdot}Al_2O_3$-$CaSO_4{\cdot}2H_2O$-$CaCO_3$-H_2O by FT-IR spectroscopy, Cem. Concr. Res. 31 (6) (2001) 869–872, https://doi.org/10.1016/S0008-8846(01)00502-6.

[74] M. Schwanninger, J.C. Rodrigues, H. Pereira, B. Hinterstoisser, Effects of short-time vibratory ball milling on the shape of FT-IR spectra of wood and cellulose, Vib. Spectrosc. 36 (1) (2004) 23–40, https://doi.org/10.1016/j.vibspec.2004.02.003.

[75] O. Hirohata, T. Wakabayashi, K. Tasaka, C. Fushimi, T. Furusawa, P. Kuchonthara, A. Tsutsumi, Release behavior of tar and alkali and alkaline earth metals during biomass steam gasification, Energ Fuel. 22 (6) (2008) 4235–4239, https://doi.org/10.1021/ef800390n.

[76] W.H. Weber, K.C. Hass, J.R. McBride, Raman study of CeO_2: Second-order scattering, lattice dynamics, and particle-size effects, Phys. Rev. B, Condensed Matter 48 (1993) 178–185, https://doi.org/10.1103/physrevb.48.178.

[77] R. Frech, E.C. Wang, J.B. Bates, The i.r. and Raman spectra of $CaCO_3$ (aragonite), Spectrochim. Acta Part A: Mol. Spectrosc. 36 (10) (1980) 915–919, https://doi.org/10.1016/0584-8539(80)80044-4.

[78] B. Zhao, B. Yan, S. Yao, Z. Xie, Q. Wu, R. Ran, D. Weng, C. Zhang, J.G. Chen, $LaFe_{0.9}Ni_{0.1}O_3$ perovskite catalyst with enhanced activity and coke-resistance for dry reforming of ethane, J. Catal. 358 (2018) 168–178, https://doi.org/10.1016/j.jcat.2017.12.012.

[79] D. Yao, H. Yang, Q. Hu, Y. Chen, H. Chen, P.T. Williams, Carbon nanotubes from post-consumer waste plastics: Investigations into catalyst metal and support material characteristics, Appl. Catal. B: Environ. 280 (2021) 119413, https://doi.org/10.1016/j.apcatb.2020.119413.